



Tunable TiO₂–BN–Pd nanofibers by combining electrospinning and atomic layer deposition to enhance photodegradation of acetaminophen

Syreina Al Sayegh, Fida Tanos, Amr Nada, Geoffroy Lesage, François Zaviska, Eddy Petit, V. Rouessac, Igor Iatsunskyi, Emerson Coy, Roman Viter, et al.

► To cite this version:

Syreina Al Sayegh, Fida Tanos, Amr Nada, Geoffroy Lesage, François Zaviska, et al.. Tunable TiO₂–BN–Pd nanofibers by combining electrospinning and atomic layer deposition to enhance photodegradation of acetaminophen. Dalton Transactions, 2022, Spotlight Collection: Atomic and Molecular Layer Deposition, 7, 10.1039/D1DT03715C . hal-03560152

HAL Id: hal-03560152

<https://hal.science/hal-03560152>

Submitted on 15 Nov 2022

HAL is a multi-disciplinary open access archive for the deposit and dissemination of scientific research documents, whether they are published or not. The documents may come from teaching and research institutions in France or abroad, or from public or private research centers.

L'archive ouverte pluridisciplinaire **HAL**, est destinée au dépôt et à la diffusion de documents scientifiques de niveau recherche, publiés ou non, émanant des établissements d'enseignement et de recherche français ou étrangers, des laboratoires publics ou privés.

Tunable TiO₂-BN-Pd nanofibers by combining electrospinning and Atomic Layer Deposition to enhance photodegradation of acetaminophen

Syreina Sayegh^{1,2}, Fida Tanos^{1,2}, Amr Nada^{1,3}, Geoffroy Lesage¹, François Zaviska¹, Eddy Petit¹, Vincent Rouessac¹, Igor Iatsunskyi⁴, Emerson Coy⁴, Roman Viter^{5,6}, Daina Damberga⁵, Matthieu Weber⁷, Antonio Razzouk², Juliette Stephan² and Mikhael Bechelany^{1*}

- 1 Institut Européen des Membranes, IEM UMR 5635, Univ Montpellier, CNRS, ENSCM Place Eugène Bataillon, 34095 Montpellier cedex 5, France.
- 2 Laboratoire d'Analyses Chimiques, LAC – Lebanese University, Faculty of Sciences, Jdeidet 90656, Lebanon.
- 3 Department of Analysis and Evaluation, Egyptian Petroleum Research Institute, Cairo, 11727, Egypt.
- 4 NanoBioMedical Centre, Adam Mickiewicz University, Wszechnicy Piastowskiej 3, 61-614 Poznan, Poland.
- 5 Institut of Atomic Physics and Spectroscopy, University of Latvia, Rainis Blvd., LV-1586, Riga, Latvia.
- 6 Center for Collective Use of Scientific Equipment, Sumy State University, 31, Sanatornaya st., 40018 Sumy, Ukraine.
- 7 Univ. Grenoble Alpes, CNRS, Grenoble INP, LMGP, F-38000 Grenoble, France.

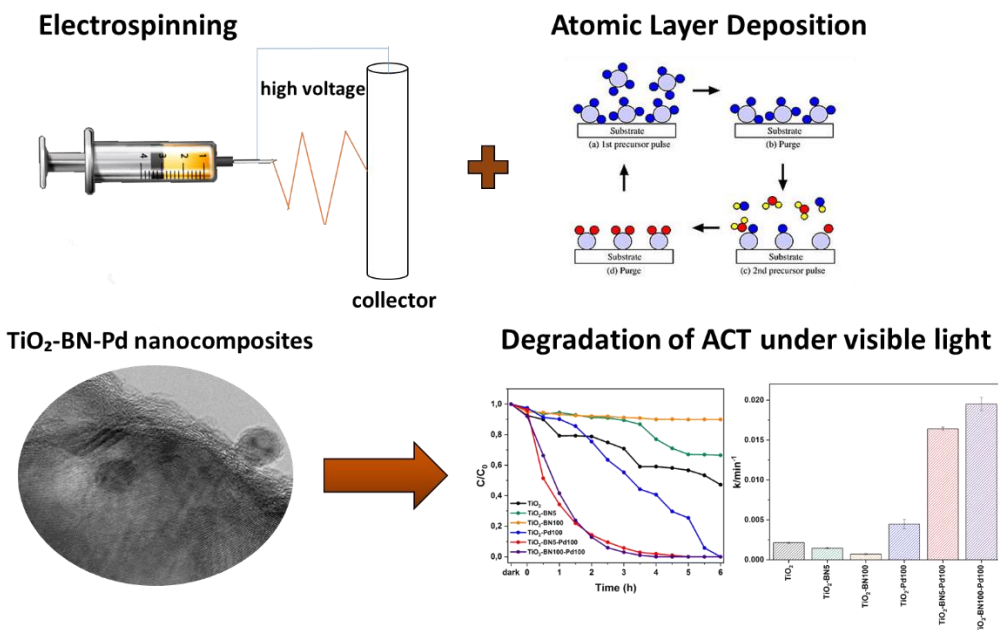
ABSTRACT

The demand for fresh and clean water sources increases globally, and there is a need to develop novel routes to eliminate micropollutants and other harmful species from water. Photocatalysis is a promising alternative green technology that has shown great performance in the degradation of persistent pollutants. Titanium dioxide is the most used catalyst owing to its attractive physico-chemical properties, but this semiconductor presents limitations in the photocatalysis process due to the high band gap and the fast recombination of the photogenerated carriers. Herein, a novel photocatalyst has been developed, based on titanium

dioxide nanofibers (TiO₂ NFs) synthesized by electrospinning. The TiO₂ NFs were coated by atomic layer deposition (ALD) to grow boron nitride (BN) and palladium (Pd) on their surface. The UV-Vis spectroscopy measurements confirmed the increase of the band gap and the extension of the spectral response to the visible range. The obtained TiO₂/BN/Pd nanofibers were then tested for photocatalysis, and showed a drastic increase of acetaminophen (ACT) degradation (>90%), compared to only 20% degradation obtained with pure TiO₂ after 4h of visible light irradiation. The high photocatalytic activity was attributed to the good dispersion of Pd NPs on TiO₂-BN nanofibers, leading to a higher transfer of photoexcited charges carriers and a decrease of photogenerated electron-holes recombination. To confirm their reusability, recycling tests on the hybrid photocatalyst TiO₂/BN/Pd have been performed, showing a good stability over 5 cycles under UV and Visible light. Moreover, toxicity tests as well as quenching tests were carried out to check the toxicity in the formation of byproducts and to determine active species responsible for the degradation. The results presented in this work demonstrate the potential of TiO₂/BN/Pd nanomaterials, and open new prospects for the preparation of tunable photocatalysts.

Keywords: TiO₂-BN-Pd nanocomposites; nanofibers, electrospinning; atomic layer deposition; photocatalysis; acetaminophen

Graphical abstract



Highlights

- TiO₂-BN-Pd materials were successfully prepared by combining electrospinning and atomic layer deposition.
- The synthesized materials were used to study the degradation of acetaminophen (ACT) under UV and visible light.
- The degradation of ACT by TiO₂-BN100-Pd100 was 80% faster than pristine TiO₂ NFs.
- The photocatalysts showed high stability and recyclability after 5 successive cycles under UV and visible irradiation.
- The main active species that play a significant role in the degradation of ACT are $\cdot\text{O}_2^-$ and h^+ .

1. Introduction

Water scarcity is a worldwide issue since the demand for clean water highly exceeds the freshwater sources.¹ To respond to this high demand, many sources of water have been considered such as wastewater, rainwater and seawater. However, these sources may contain harmful contaminants such as dyes, pesticides, pharmaceuticals and personal products, considered "emerging pollutants" ². Additionally, conventional wastewater treatment methods are inefficient in removing persistent organic substances such as drugs from the water and the presence of such contaminants, even at low concentrations, may be harmful on human health and aquatic organisms ³⁻⁵. Many new techniques have been developed to overcome these limitations, such as ozonation, electrooxidation, photo-Fenton and photocatalysis^{6,7}. Photocatalysis has attracted much attention in the last decades as a promising approach for water treatment ^{8,9}. It is an advanced oxidation process, based on the excitation of a semiconductor that will engender electron-hole pairs responsible of the degradation of pollutant^{10,11}. Therefore, it is considered as an effective technique to remove trace contaminants and their intermediates products that could be more harmful ^{12,13}.

In recent years, semiconductor photocatalysts have been considered for environmental and energy applications for catalytic and sensing purposes¹⁴⁻¹⁶. Among most of the semiconductors used in photocatalysis, titanium dioxide (TiO₂) has retrieved much attention for the removal of organic pollutants from wastewater. TiO₂ has several advantages regarding its high photocatalytic efficiency, high stability, low toxicity and low cost ¹⁷⁻¹⁹. However, the wide band gap (~ 3.0-3.2 eV) limits the application of this photocatalyst under visible light. Another disadvantage is the fast recombination of photogenerated carriers, limiting its usages in large scale²⁰⁻²².

During the last years, research has focused on designing hybrid nanocatalysts and heterostructures to conquer TiO₂ limitations²³⁻²⁶. Many studies have been presented, such as doping with metal ions (Pd, Ag, Pt...)^{10,27-30}, nonmetal ions (B, N, Cu, Ni...)^{31,32}, and creation of heterojunctions with other semiconductors (BN, ZnO, CuO)³³⁻³⁵. Coupling TiO₂ with other semiconductors or metals will allow the formation of heterojunction that can increase the lifetime carrier charge, reduce the recombination of electron holes, and improve the photocatalysis efficiency of TiO₂ under visible light^{36,37}.

Many studies have reported the efficiency of doping TiO₂ with BN for dyes and pollutant degradation since BN has a high ability of energy storage to allow higher e⁻-h⁺ transfers and a high chemical stability^{38,39}. Nasr *et al.* reported that TiO₂-BN nanocomposites synthesized by electrospinning enhanced the degradation of methyl orange under UV light. They confirmed that BN could improve the photocatalytic activity of TiO₂ due to the immigration of holes to the catalyst surface¹⁰. The photocatalytic oxidation of ibuprofen by TiO₂-BN nanocomposites were also studied by Lin *et al.*⁴⁰. The photodegradation of ibuprofen was enhanced due to the incorporation of BN, and a complete degradation was obtained after 2h of UV irradiation. Sheng *et al.* prepared hexagonal boron nitride (h-BN)/titania (TiO₂) nanocomposites by sol-gel. They reported the degradation of rhodamine B (RhB) and methylene blue (MB) under UV light irradiation of 98% and 92% within 50 min irradiation, respectively⁴¹.

In addition, loading noble metals such as palladium (Pd), platinum (Pt) and silver (Ag) on the surface of the substrate, appears to be effective for the elaboration of potential catalysts^{42,43}. These metal nanoparticles (NPs) will allow the improvement of visible light excitation and reduce the recombination of e⁻/h⁺ pairs due to the surface plasmonic resonance effect and the metals' performance as charge acceptors, respectively⁴⁴. Among these metals, loading Pd on the surface of TiO₂ has proven to be an effective method to improve visible light photocatalytic degradation. Mohapatra *et al.* prepared TiO₂-NTs with well-dispersed Pd NPs by incipient wetness method. The catalyst has shown effective degradation of dyes under solar light simulator⁴⁵. Moreover, photocatalytic oxidation of nitrogen oxide (NO) was successful using Pd-modified TiO₂ prepared by thermal impregnation method⁴⁶.

Most of these studies have used several techniques such as electrospinning²², sol-gel method⁴⁷, microwave-assisted synthesis⁴⁸, etc. Since visible photocatalysts are required for efficient catalytic applications, a highly structured material with a large specific area and more exposed active sites should be designed⁴⁹. To our knowledge, no degradation of acetaminophen (ACT) was reported with TiO₂-BN-Pd nanocomposites. The major challenge is to design a semiconductor catalyst with a well-known structure, precise morphology and high selectivity.

Atomic layer deposition (ALD) combined with electrospinning shows potential advantages in fabricating highly effective and selective photocatalysts.

ALD is a vapor deposition technique that allows the preparation of thin films in the sub-nanometer scale with precise thickness and high conformality^{50,51}. ALD enables the synthesis of nanoparticles and thin films with controllable dimensions at the subnanoscale, a unique capability^{52–57}. The use of ALD in catalysis field is getting more attention since it enables the design of nanocatalyst with control over size, composition, thickness and distribution of the material⁵⁸. For example, Weber *et al.* reported the synthesis of carbon paper-boron nitride-palladium electrodes using ALD, which electrochemical active surface was maintained stable even after applying an accelerated ageing program for 1000 cycles⁵⁹.

In their recent review, Vempati *et al.* reported the importance of the combination of ALD with electrospinning in the elaboration of catalytic materials⁶⁰. Electrospinning is an easy technique to fabricate NFs with a controlled diameter in a range between 10-1000 nm, by applying a high electric field between the polymeric solution and the collector^{61,62}. Preparation of TiO₂ nanofibers by electrospinning has been widely used, since electrospinning allows the fabrication of many nanostructures with low aggregation, high porosity, and large specific surface area, which can promote the charge and mass transfer for enhanced photocatalytic activities^{63,64}.

Recently nanocomposite materials for photocatalysis degradation of pharmaceuticals pollutants have involved many research studies^{65–67}. Herein, we report for the first time the degradation of ACT with TiO₂-BN-Pd catalyst obtained by combining two major techniques, electrospinning and ALD. First, TiO₂ was synthesized by electrospinning, followed by a uniform deposition of BN by ALD. Pd nanoparticles was then added to obtain hybrid catalysts. Moreover, a variation of BN deposition cycles was also performed, and the degradation of ACT used as a model pollutant was compared under UV and visible light. TiO₂-BN100-Pd100 hybrid photocatalyst has shown the best photocatalytic activity among all prepared catalysts. Moreover, the catalyst has shown high stability even after 5 cycles. The toxicity was also evaluated during the degradation process to ensure that harmful byproducts generated during the process were degraded as well. Finally, scavengers study was conducted to get an idea about the mechanism

of degradation of ACT. The main species responsible of the degradation of acetaminophen were holes and superoxide radicals.

2. Experimental

2.1. Materials and chemicals

Titanium(IV) isopropoxide (TTIP, 97%, CAS: 546-68-9), polyvinyl pyrrolidone (PVP, Mw=1300000, CAS: 9003-39-8), acetaminophen (ACT, ≥99% CAS: 103-90-2), formaline solution (HCHO, CAS: 50-00-0), boron tribromide (BBr₃, 99.9%, CAS: 10294-33-4), nafion perfluorinated resin solution (CAS: 31175-20-9), sodium sulfate (Na₂SO₄, ≥99%, CAS: 7757-82-6), sodium chloride (NaCl, ≥99%, CAS: 7647-14-5), 2-propanol (99.9%, CAS: 67-63-0), p-benzoquinone (C₆H₄O₂, ≥99.5%, CAS: 106-51-4) and ethylenediaminetetraacetic acid (EDTA, 99.995%, CAS: 60-00-4) were purchased from Sigma-Aldrich. In addition, Pd palladium(II) hexafluoroacetylacetonate (≥95%, CAS: 64916-48-9) was purchased from Strem Chemicals. Acetic acid (CAS: 64-19-7) and ethanol (≥99.8% CAS: 64-17-5) were purchased from VWR chemicals and used as solvents. All chemicals were used without further purification. Indium tin oxide (ITO) deposited on quartz was purchased from Präzisions Glas & Optik. Deionized (DI) water (>18.2 MΩ) prepared by Millipore (Milli-Q® Academic) water purification system was used for all dilutions and reagent preparation. Argon gas and ammonia were bought from Linde and used as received.

2.2. Synthesis of TiO₂ nanofibers by electrospinning

The preparation of TTIP/PVP solution was similar to previous studies as shown in *Figure 1*¹⁹. Acetic acid and ethanol are used as solvents. The suspension was stirred for 2h prior to spinning in order to increase the dielectric constant and obtain an electrospinnable solution. The resulting solution was then loaded in a 22 mL syringe and electrospun by a homemade electrospinning system. During the process, a high voltage of 25 kV and a flow rate of 1mL/h were applied. The distance between the 19 gauge needle and the collector was fixed at 10 cm. When the electric field is created, the polymer jet between the droplet and the grounded collector leads to fibres forming, overcoming the surface forces^{68–70}. This process was followed by calcination of obtained fibers at 400°C for 4h to remove the polymer and obtain crystalline TiO₂.

2.3. Modification of TiO₂ by Atomic Layer Deposition

2.3.1. Atomic Layer Deposition of Boron Nitride

The coating of BN was carried out on electrospun nanofibers at 750°C in a low-pressure homemade ALD reactor. The reactor was directly connected to the precursor and co-reactant lines through gate valves and heated at 110°C to avoid condensation. The deposition of BN was achieved using sequential exposures of BBr₃ and NH₃ (considered as co-reactant) separated by purge steps of argon with a flow rate of 100 sccm. One ALD cycle consisted of a 0.1 s BBr₃ pulse, 5 s exposure, and 15 s Ar purge, followed by a 5 s NH₃ pulse, 5 s exposure, and 20 s Ar purge. More details on the ALD reactor and on the process are listed elsewhere⁵. In order to adjust the BN loading, the number of ALD cycles was varied. Thicknesses of deposited BN were characterized by ellipsometry on Si substrates added in the same of NFs using an optical model based on Cauchy fitting model (Semilab spectroscopic ellipsometer GES5E, Xe lamp 1.23eV-5eV).

2.3.2. Atomic Layer Deposition of Palladium

TiO₂-Pd were synthesized by atomic layer deposition in a low-pressure hot-wall (home-built) reactor, described earlier^{71,72}. ALD of Pd was carried out with Pd(hfac)₂ and formalin. The highly dispersed Pd NPs were synthesized by applying 100 ALD cycles. The bubbler containing the Pd(hfac)₂ precursor was heated at 70 °C and the formalin container was kept at room temperature. The deposition chamber was set at a temperature of 220 °C, and the lines in the ALD system were heated at 80 °C to avoid any condensation⁷³. The ALD cycle consisted of sequential pulse, exposure, and purge of Pd precursor and formalin, alternatively. The pulse, exposure, and purge durations were 5:15:10 s and 1:15:60 s for Pd(hfac)₂ and formalin, respectively.

2.4. Characterization of the synthesized nanocomposites

A Hitachi S4800 emission scanning electron microscope (SEM, JAPAN) was used for morphology measurements of synthesized nanofibers. All samples were sputter coated with platinum/palladium before SEM measurement using a Polaron SC7620 Mini Sputter Coater. The

crystal phases of the samples were examined by XRD diffractometer using Cu-K α radiation ($\lambda=1.5406$ Å) in 2θ ranging from 10 to 80°. Fourier-transform infrared spectroscopy (FTIR) of TiO₂, TiO₂-BN, TiO₂-Pd and TiO₂-BN-Pd nanocomposites was recorded with the NEXUS instrument, equipped with an attenuated total reflection accessory in the frequency range of 400–4000 cm⁻¹. Raman spectra were measured by the dispersive Raman spectroscopy (Horiba XploRA), using a 659.55 nm laser and an objective lens of 100. Transmission electron microscopy (TEM) was performed using JEOL 2200FS (200 kV) and JEOL ARM-200F (200kV). X-ray photoelectron spectroscopy (XPS) measurements were conducted via ESCALAB 250 spectrometer from Thermo Electron using Al K α monochromatic source (1486.6 eV) as an excitation source. In order to determine the band gaps of synthesized materials, the UV-vis spectra were measured by a UV-vis spectrophotometer (Jasco model V570) equipped with a diffuse reflectance (DR) attachment (Shimadzu IRS-2200) for optical absorbance measurements. Photoluminescence (PL) spectra were recorded with an optical fiber spectrometer (Ocean Optics usb2000) with an excitation wavelength of 266 nm by a nitrogen Nd:YAG laser, 9mW.

2.5. Electrochemical impedance spectroscopy measurement

An electrochemical system was used to carry out the EIS tests by a Solartron SI 1287 potentiostat/ galvanostat. Three-electrode cell were used to study the photoelectrochemical property: photocatalysts used as working electrode, Ag/AgCl as reference electrode and platinum wire as counter electrode immersed in Na₂SO₄ solution (0.1 mol/L) considered as electrolyte. The mixtures of 4 mg photocatalyst, 1 mL isopropanol and 40 μ L nafion aqueous solution were homogeneously mixed by the ultrasonic cleaner for 30 min, then the slurry was dropped on the ITO glass (1x1cm), and the working electrode was achieved after the evaporation of isopropanol. Moreover, the measurements were done using a 150 W halogen lamp as the light source under visible light exposition.

2.6. Quantum efficiency measurements

The measurements were performed in the following way:

3.5 mL plastic cuvette was filled with 2.5 mL of mQ water and installed into a cuvette holder. Tungsten light source (Avantes) was used for absorbance measurements. The 1 mg.mL⁻¹ water solutions of TiO₂-X samples were prepared. 50 mL of solution was added to the cuvette and absolute irradiance spectra of the sample were recorded (*Figure S1*).

According to Kubelka-Munk following equations are applicable for the calculation of quantum efficiency:⁷⁴

$$R_{\infty} = \frac{(1+R_0^2-T^2)-\left((1+R_0^2-T^2)^2-4R_0^2\right)^{0.5}}{2R_0} \quad (1)$$

Where K, S, T, R₀, d are diffuse absorption coefficient, diffuse scattering coefficient, transmittance (%), reflectance (%) and sample thickness (cm).

Within this theory, absorption and scattering coefficients can be calculated, the detailed calculation is represented in supporting information⁷⁴.

The quantum efficiency for 1 cm³ volume of 0.5 mg.mL⁻¹ photocatalyst solution was calculated as following equation 2:

$$QE = \frac{N_0 - N}{\sum_{400\text{ nm}}^{700\text{ nm}} \eta(\lambda) \cdot N_{ph}(\lambda)} \quad (2)$$

Where N₀, N, η(λ) and N_{ph}(λ) are the initial concentration of organic molecules (cm⁻³), concentration of organic molecules after 3 hours of exposure to visible light (cm⁻³), part of absorbed light and number of incident photons (cm⁻²) for wavelength λ.

2.7. Photocatalytic experiments of acetaminophen

Photocatalytic activity of the synthesized nanocomposite was evaluated on the degradation of acetaminophen under two light sources. A medium pressure metal halide UV lamp (400 W, Lampes France) and a visible light source provided by a linear halogen lamp (400W, Avidé) were used for the comparative study. The irradiation distance between the lamp and the sample was fixed to 10 cm for all experiments.

The photocatalysts (0.5 g.L⁻¹ - TiO₂, TiO₂-BN, TiO₂-Pd and TiO₂-BN-Pd) were added into 250 mL of ACT solution (1 mg.L⁻¹) in a 300 mL glass reactor. A water bath was used to minimize the temperature increase in the solution under the light irradiation and keep it stable at 37 °C. The solution was stirred for 30 minutes to ensure equilibrium adsorption in the dark and then exposed to irradiation. At certain time intervals, 3 ml aliquots were sampled and filtered with 0.22 µm filters. The ACT concentration was analyzed by high-performance liquid chromatography equipped with a C-18 column (RP18, Nucleoshell) and a Quattro-Micro mass spectrometer with an Electrospray probe (Waters Micromass, Wythenshawe, Manchester, UK) as a detector. An isocratic method (A/B=97/3) set at 0.25 mL.min⁻¹ flow rate was used. The phase A of eluents consisted of a mixture of acetonitrile/water (95/05), while the phase B was 100 % acetonitrile with 0.1 % formic acid for both phases.

The recyclability of the catalyst that showed the best degradation efficiency was further investigated. The nanocomposite was reused under UV and visible light for 5 cycles with the same initial conditions.

The degradation efficiency (D(%)), was calculated according to Eq. (3):

$$D(\%) = [(C_0 - C)/C_0] \times 100 \quad (3)$$

where: C₀ and C are the initial and final concentrations at mg.L⁻¹.

2.8. Photocatalytic kinetic model

Typically, TiO₂ kinetics is usually characterized by Langmuir–Hinshelwood (L–H) model^{40,75}. When the concentration of the pollutant is low, pseudo-first-order kinetics is applied⁷⁶, Eq.(4):

$$\ln (C_0/C) = kt \quad (4)$$

where C₀ (mg.L⁻¹) is the initial concentration of the pollutant, C is the pollutant concentration at time t (min) and k (min⁻¹) is the pseudo-first-order rate constant.

2.9. Microtoxicity tests for determination of byproducts toxicity

During the degradation of acetaminophen, many byproducts could be formed ⁷⁷. In order to confirm or not the toxicity of these compounds, a bioluminescence toxicity study was carried out. This study is based on the measurements of the luminescence effect of marine bacteria. The bacteria used in this method was the strain *Vibrio fischeri* LCK 487. All measurements were conducted using Microtox® Model 500 Analyzer (Modern Water Inc.; United Kingdom) coupled with MicrotoxOmni® software. First, the bacteria reconstitution was performed by adding 5mL of the reagent diluents at 5°C. Then 200 µL of the solution was transferred to the cuvettes, and the reagent was stabilized at 15°C for 15 min. In order to enhance the activity of *Vibrio Fischeri* bacteria, the samples were diluted at 81.8% of initial concentration by adding 22% NaCl solution. Based on luminescence intensity, the screening test 81.8% allow identifying samples toxicity. Bacteria's activity could be reduced by the presence of toxic elements that decrease luminescence. Before measuring the bacteria luminescence, all the samples were filtered with 0.2 mm filters to remove any precipitate or solid matter in the solution. The toxicity values are directly relative to the inhibition rate of bacteria's activity, calculated as following in equation (5)^{77,78}:

$$Ic_{(t)}(\%) = \left(1 - \frac{LU_{(t)}}{LU_{(0)} \times R_{(t)}}\right) \times 100 \quad (5)$$

where $LU_{(t)}$ is the intensity of luminescence emitted by bacteria after $t=15$ min of contact with the sample; $LU_{(0)}$: is the initial intensity of luminescence emitted by bacteria before the addition of the sample; $R_{(t)}$: is the corrected term.

Since luminescence of bacteria decreases over time and under the action of environmental conditions in the absence of toxicity, it is necessary to compensate for the errors due to these factors by taking into account the variability of the luminescence $R_{(t)}$ of the bacteria in a control solution (MilliQ water and NaCl) which gives the LU_0 values. The corrected term is given by equation (6):

$$R_{(t)} = \frac{LU_{0(t)}}{LU_0} \quad (6)$$

where $LU_{0(t)}$ is the intensity of luminescence emitted by bacteria after a $t=5$ min or $t=15$ min of contact with the control solution (MilliQ water and NaCl); and LU_0 : is the initial intensity of

luminescence emitted by bacteria before the addition of the control solution (MilliQ water and NaCl).

2.10. Quenching tests

Scavengers test were performed in order to determine the main active species responsible of the degradation of ACT. Benzoquinone, isopropanol and EDTA were added to the solution at 10, 5 and 17 mM, respectively, before switching the light on. The experiments performed was the same as the degradation process, an aliquot was withdrawn at different times and LC-MS-MS detected the concentration of ACT.

3. Results and discussion

3.1. Characterization of synthesized nanocomposites

TiO₂-BN-Pd photocatalysts were prepared in three steps, as illustrated in *Figure 1* In the first step, TiO₂ nanofibers (NFs) were prepared by electrospinning than calcinated at 400°C under air. *Figure 2* shows the scanning electron microscopy image of TiO₂ NFs after calcination. It can be clearly seen that we have continuous and randomly oriented nanofibers that preserved their morphologies after calcination. In the second step, atomic layer deposition was used to modify the surface of the prepared NFs. First, we have coated TiO₂ with a second semiconductor, Boron Nitride, at 750°C. To compare the effect of BN, we varied the BN number of cycles (5 and 100 cycles) for a thickness variation with BN having a gpc on Si substrate of 0.8 nm. The as-prepared samples will be designated by TiO₂-BN5 and TiO₂-BN100, respectively. In the last step, a deposition of 100 cycles of Pd has been processed on pure TiO₂ NFs and TiO₂-BN composites (donated as TiO₂-Pd100, TiO₂-BN5-Pd100 and TiO₂-BN100-Pd100). The BN coating has been used to enhance the separation of charge carriers as for Pd, it was added to allow the shift of band gap in the visible. Nanofibers with diameter range between 50 and 400 nm with length of several microns were obtained.

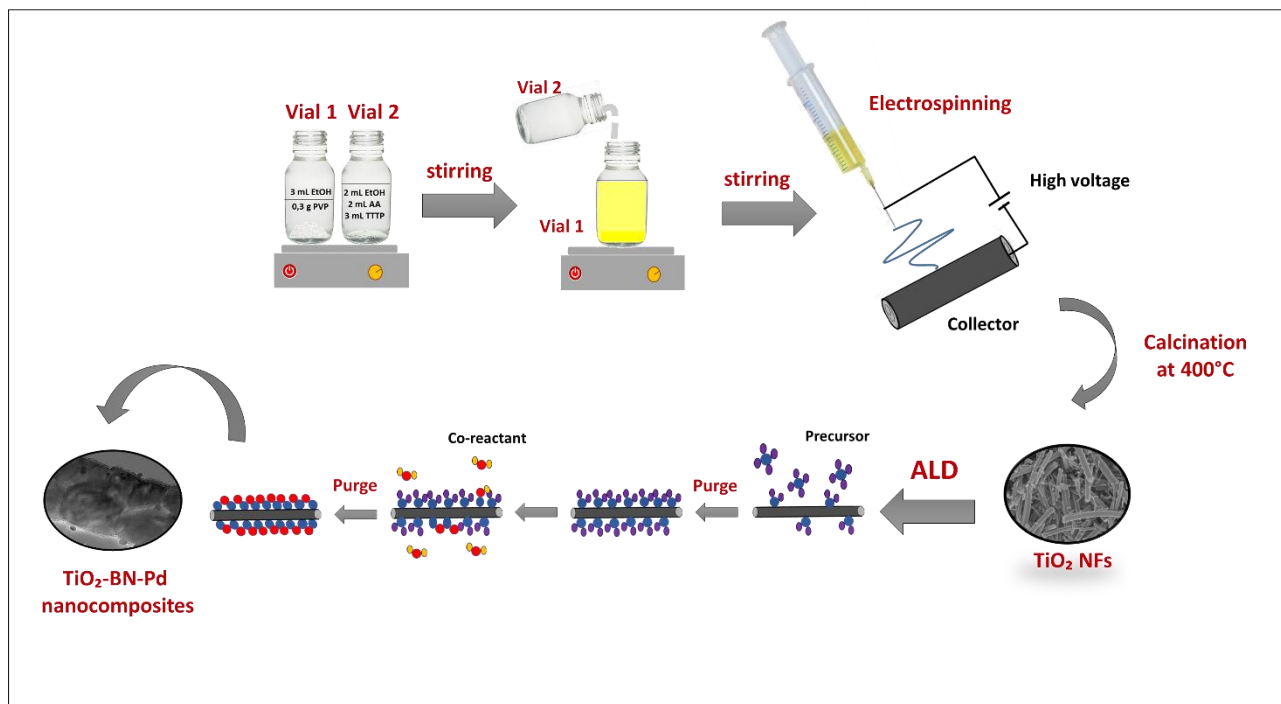


Figure 1. Illustration of the steps for the preparation of nanocomposites, in the first step we prepared the polymeric solution, then electrospinning was performed. The collected nanofibers were then calcined before ALD process.

SEM images of nanocomposites $\text{TiO}_2\text{-BN5}$, $\text{TiO}_2\text{-BN100}$, $\text{TiO}_2\text{-Pd100}$, $\text{TiO}_2\text{-BN5-Pd100}$ and $\text{TiO}_2\text{-BN100-Pd100}$ (Figure 2) show that after ALD deposition, the continuous morphology of TiO_2 was maintained. Nevertheless, when BN deposition increased from 5 to 100 cycles, the surface of TiO_2 NFs became rougher.

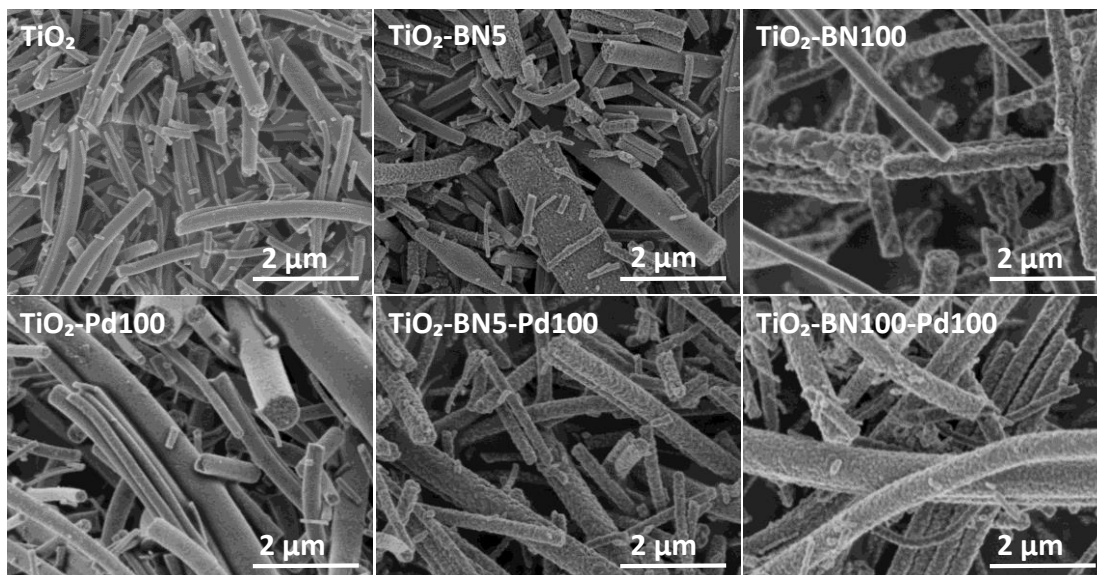


Figure 2. SEM images of TiO_2 , $\text{TiO}_2\text{-BN5}$, $\text{TiO}_2\text{-BN100}$, $\text{TiO}_2\text{-Pd100}$, $\text{TiO}_2\text{-BN5-Pd100}$ and $\text{TiO}_2\text{-BN100-Pd100}$ nanocomposites.

In order to get a closer idea about the crystallinity of the prepared catalysts, XRD analysis were conducted. According to the XRD patterns (*Figure 3 a*), pure TiO_2 obtained by electrospinning and calcinated at 400°C shows a major peak at 25.3° , corresponding to anatase (101) plane. Furthermore, a small peak at 27.4° is assigned to rutile (110). XRD peaks at 25.3° , 37.9° , 48.2° , 55.1° and 62.9° 2θ diffraction angles were assigned to anatase (101), (004), (200), (211) and (204) crystal planes, whereas XRD peaks at 27.5° , 36.2° , 41.3° , 44.1° , 54.4° , and 69.1° were assigned to rutile TiO_2 (110), (101), (103), (100), (211) and (220) crystalline planes¹⁷.

The concentration of rutile phase was determined using the spurr equation:

$$F_R = 1 / (1 + 0.8 [I_A(101) / I_R(110)]) \quad (7)$$

Where I_A and I_R are the integrated intensities of the diffraction peaks for anatase (101) and rutile (110) phases, respectively⁷⁹.

The anatase and rutile fractions were calculated for all the prepared samples. TiO_2 NFs was composed from 70.5% anatase phase while the anatase fraction varied for doped samples, the fraction was in a range between 43.6% ($\text{TiO}_2\text{-BN100}$) and 67.1% ($\text{TiO}_2\text{-Pd}$). The values of anatase/

rutile phase are represented in *Table 1*. This decrease in anatase rate in TiO₂-BN100 is due to BN deposition at high temperatures (750°C) where the anatase is no more stable. Anatase was proved to be the most active phase for photocatalytic degradation due to the lower rates of recombination and higher surface adsorptive capacity of anatase than that of rutile⁸⁰. However, many studies confirmed that a mixture of crystalline phases 30% rutile and 70% anatase make the best photocatalyst for the oxidation of organics when applied to treat wastewater⁸¹. Hence, crystallinity is not the only parameter to be considered, many other factors could affect the activity and selectivity of photocatalysts, such as surface structure, surface defects, and surface charge⁸².

In addition, diffraction peaks of Pd species were not depicted. According to the literature, Pd species, (Pd⁰ or PdO) could not be detected by XRD due to low dopants concentration; highly dispersed NPs on the support or overlapping of Pd peaks with TiO₂⁸³. For BN, the diffraction peak at 2θ = 26° of hexagonal BN related to the (002) direction has not been observed too, it is probably overlapped with the diffraction peak of TiO₂ at the same position¹⁰. Moreover, the grain sizes of the TiO₂ dominating phase crystals were calculated to be 11.5, 11.6, 23.5, 32.4 nm, 28.2 nm and 35.3 for TiO₂, TiO₂-Pd, TiO₂-BN5, TiO₂-BN100, TiO₂-BN5-Pd100 and TiO₂-BN100-Pd100, respectively, based on the Scherrer equation described below:

$$D = \frac{K\lambda}{\beta \cos \theta} \quad (8)$$

Where D is the crystallite size (nm); K is the Scherrer constant, 0.9; λ, is the X-ray wavelength, 0.15406 nm; β is the full-width at the half maximum intensity of the peak, in radians; and θ is the diffraction angle⁸⁴. It can be concluded that the crystallite size increased remarkably when adding BN.

The increase in crystallite size when doping with BN could be due to the incorporation of B/N in the lattice of TiO₂ or to the higher deposition temperature of BN at 750°C and/or the generation of oxygen vacancies inside the TiO₂ lattice^{85,86}. To confirm these results TEM and XPS has been performed and discussed below.

Figure 3b shows the Raman spectrum of TiO_2 , $\text{TiO}_2\text{-BN5}$, $\text{TiO}_2\text{-BN100}$, $\text{TiO}_2\text{-Pd}$, $\text{TiO}_2\text{-BN5-Pd100}$ and $\text{TiO}_2\text{-BN100-Pd100}$. The Raman active mode revealed the characteristic peaks of both crystalline phases of TiO_2 , anatase and rutile, confirming the XRD results. For all samples, we observe peaks corresponding to the active mode of anatase phase at 151 and 203 (E_g), 513 (B_{1g} , A_{1g}) and 638 (E_g) cm^{-1} . In addition, nanocomposites samples shows three peaks corresponding to the active modes of rutile phase at 258 cm^{-1} (B_{1g}), 447 cm^{-1} (E_g) and 633 cm^{-1} (A_{1g})^{12,78}. Furthermore, Figure 3 c shows the raman spectra of $\text{TiO}_2\text{-BN100}$, with a small band at 1328 cm^{-1} that could be attributed to h-BN active mode⁷.

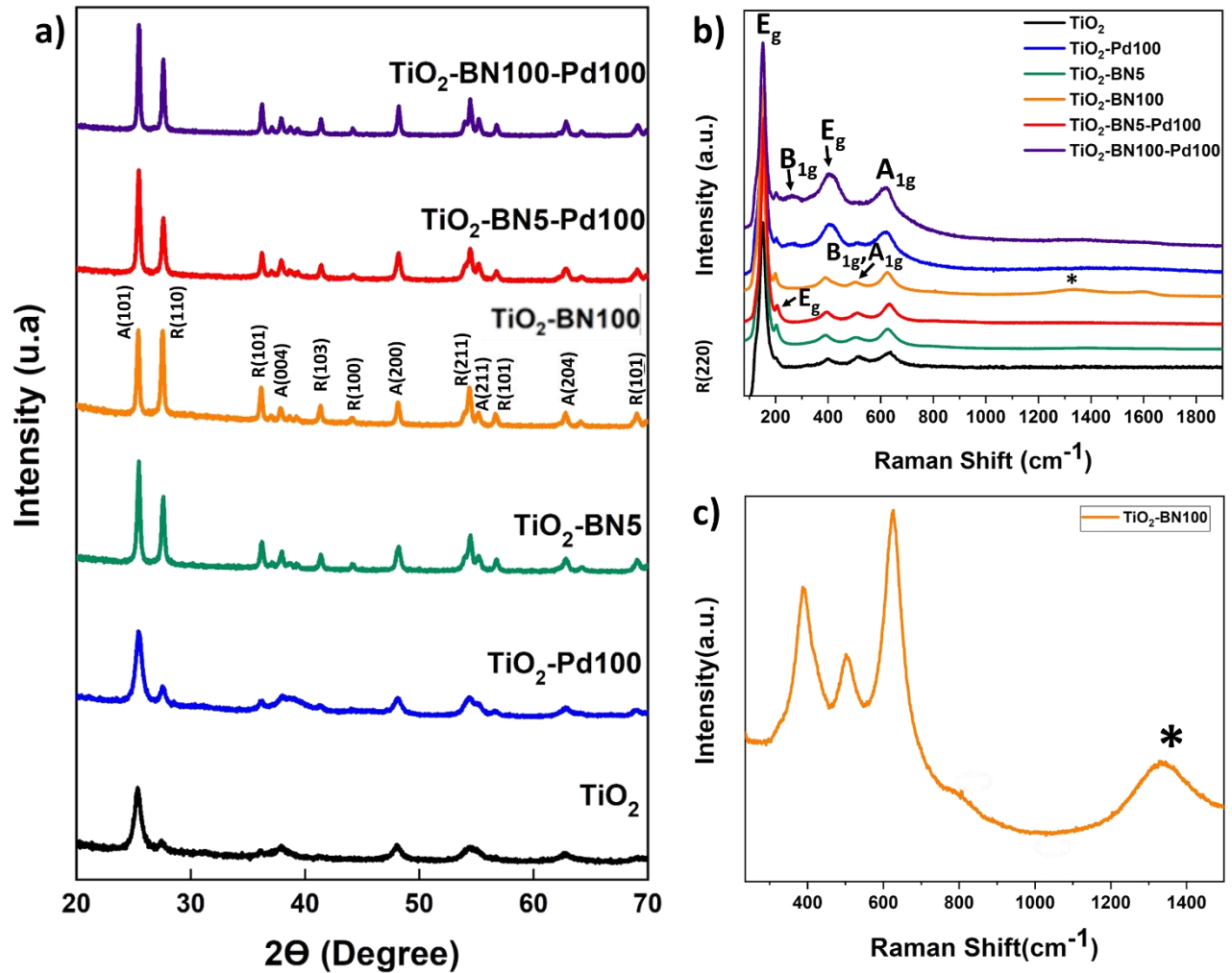


Figure 3. a) XRD data b) Raman spectra of bare TiO₂ and synthesized nanocomposites and c) zoom on Raman spectra of TiO₂-BN100.

In addition to Raman and XRD spectra, Infrared spectroscopy was performed to confirm the functional groups of the prepared NFs. *Figure S2* shows the characteristic absorption band of as-prepared samples. The large band at 800–1200 cm⁻¹ is attributed to Ti–O bond. For TiO₂-BN100 and TiO₂-BN100-Pd100 in-plane B–N optical mode (1373 cm⁻¹) was observed. No peaks could be detected in TiO₂-BN5 and TiO₂-BN5-Pd100, due to the low amount deposited by ALD (less than 0.5nm) and/or the incorporation of BN into the lattice of TiO₂.

Since none of the characterization techniques listed above has confirmed the deposition of Pd, high-resolution transmission electron microscopy (HRTEM) was employed. The state of dispersion of metal Pd particles and BN was examined by TEM for TiO₂-Pd100, TiO₂-BN5-Pd100 and TiO₂-BN100-Pd100. TEM images of TiO₂-Pd100, TiO₂-BN5-Pd100 and TiO₂-BN100-Pd100 photocatalysts (*Figure 4*), shows that Pd NPs are dispersed uniformly on the surface of TiO₂ NFs. The dispersion of Pd decreases with the increase of BN thickness, this could be explained by the nucleation of the precursor on BN surface and/or to the decrease of the nucleation sites. The HRTEM image of *Figure 4c* shows that the Pd NPs are deposited on the surface lattice of TiO₂. Mackus *et al.* demonstrated that keeping the sites of TiO₂ catalysts available and depositing particles on preferential sites would enhance the selectivity of the synthesized catalysts⁵². The diameter of Pd NPs was in the range of 1 to 5nm. In *Figure 5f*, the boron nitride layer of TiO₂-BN5-Pd100 sample could not be detected by EDX due to the low deposition rate and since Boron is a light element that could not be easily detected by this technique. For TiO₂-BN100-Pd100, *Figure 4.i*, the HRTEM image indicate that TiO₂ is covered by a layer of ~7nm of BN. Additionally, *Figure 4f* displays the SAED with a lattice spacing of 0.344 nm, which corresponds to the anatase (101), while a *d*-spacing of 0.208nm is attributed to the Pd (111).

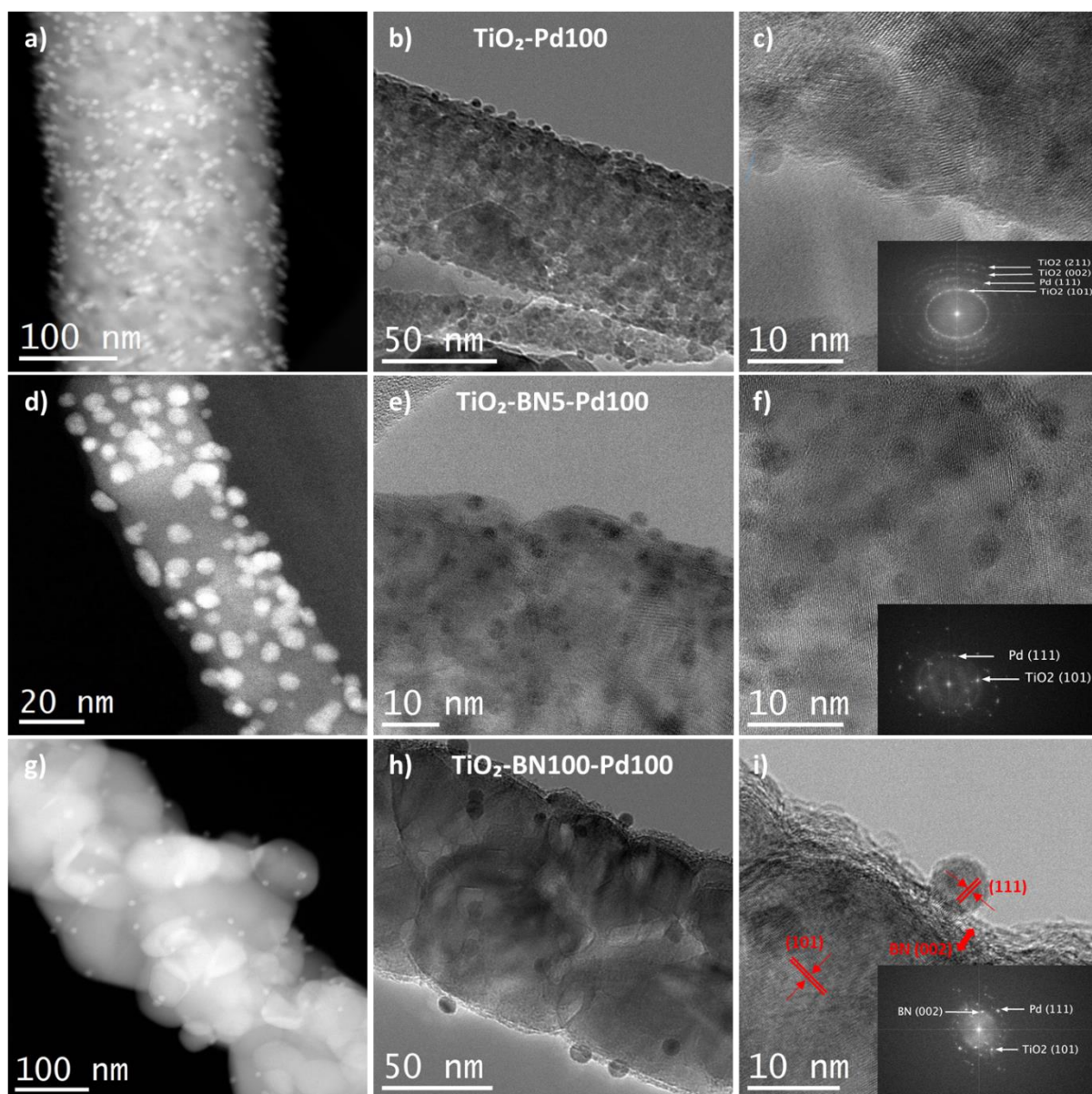


Figure 4. TEM and HRTEM images of (a-c) $\text{TiO}_2\text{-Pd100}$; (d-f) $\text{TiO}_2\text{-BN5-Pd100}$ and (g-i) $\text{TiO}_2\text{-BN100-Pd100}$.

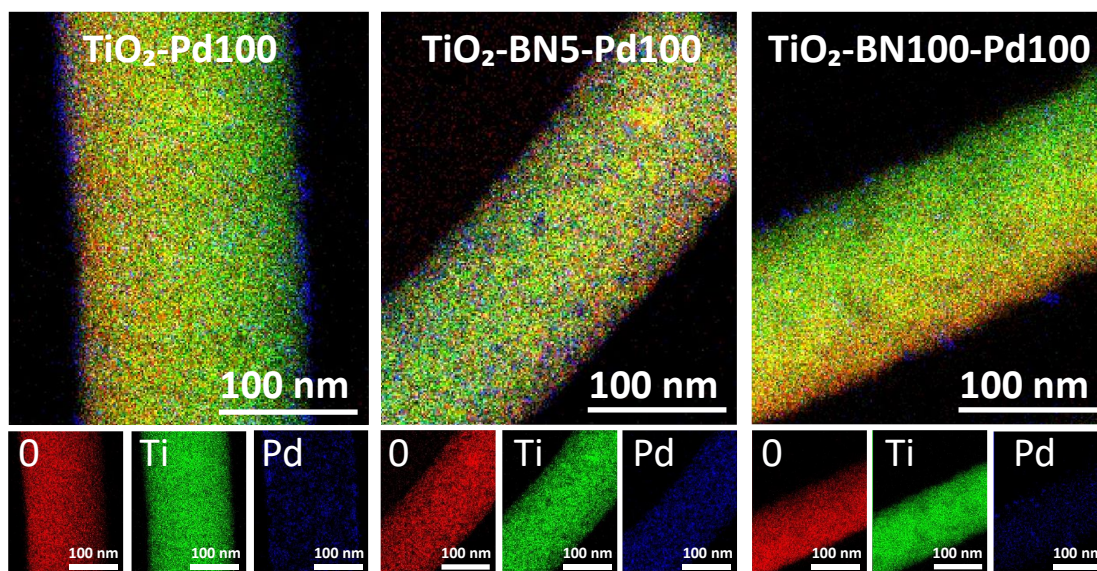


Figure 5. EDS Elemental mapping of $\text{TiO}_2\text{-Pd100}$, $\text{TiO}_2\text{-BN5-Pd100}$ and $\text{TiO}_2\text{-BN100-Pd100}$ nanofibers.

As the obtained $\text{TiO}_2\text{-BN-Pd}$ nanocomposites were designed and prepared for photocatalytic purposes, it is important to know the chemical state of each element via composition analysis using XPS technique. *Figure S2a* shows the survey spectra of $\text{TiO}_2\text{-BN100-Pd100}$, all elements were clearly seen. *Figure 6a* shows the Ti 2p XPS spectra of pure TiO_2 , $\text{TiO}_2\text{-BN100}$, $\text{TiO}_2\text{-Pd100}$, $\text{TiO}_2\text{-BN5-Pd100}$ and $\text{TiO}_2\text{-BN100-Pd100}$ composites. For Ti 2p in TiO_2 sample, two peaks are positioned at 458.7 and 464.4 eV, corresponding to $\text{Ti } 2p_{3/2}$ and $\text{Ti } 2p_{1/2}$ states indicating that Ti is 4+ valence. For the $\text{TiO}_2\text{-BN}$ and $\text{TiO}_2\text{-Pd}$ samples, Ti 2p peaks are slightly shifted toward higher binding energy (+0.2 eV and + 0.3 eV) due to the inclusion of BN and Pd, respectively, into the TiO_2 lattice and the formation of oxygen vacancies exhibiting a high electron-attracting effect⁸⁸. Similar behavior were observed for O 1s spectrum (*Figure 6b*). Considering TiO_2 spectrum as reference, O 1s spectra of TiO_2 show a peak at 529.9 eV attributed to Ti-O bond, while $\text{TiO}_2\text{-BN100-Pd100}$ shows two characteristic peaks at a higher binding energy 530.1 eV attributed to Ti-O bonds and at 532.6 corresponding to B-O-Ti groups. *Figure S3b* shows the deconvolution peaks of O 1s element for all samples. Doping TiO_2 with BN and Pd reduced the atomic percentage of Ti-O-Ti and generated new boron nitride bonds in the case of $\text{TiO}_2\text{-BN100}$ and more OH groups in the case of $\text{TiO}_2\text{-Pd100}$. For the samples with BN coating (*Figure 6 c-d*), the B 1s and

N1s elements are identified. The peaks position of B 1s and N1s are shifted to higher binding energy when incorporating Pd NPs.

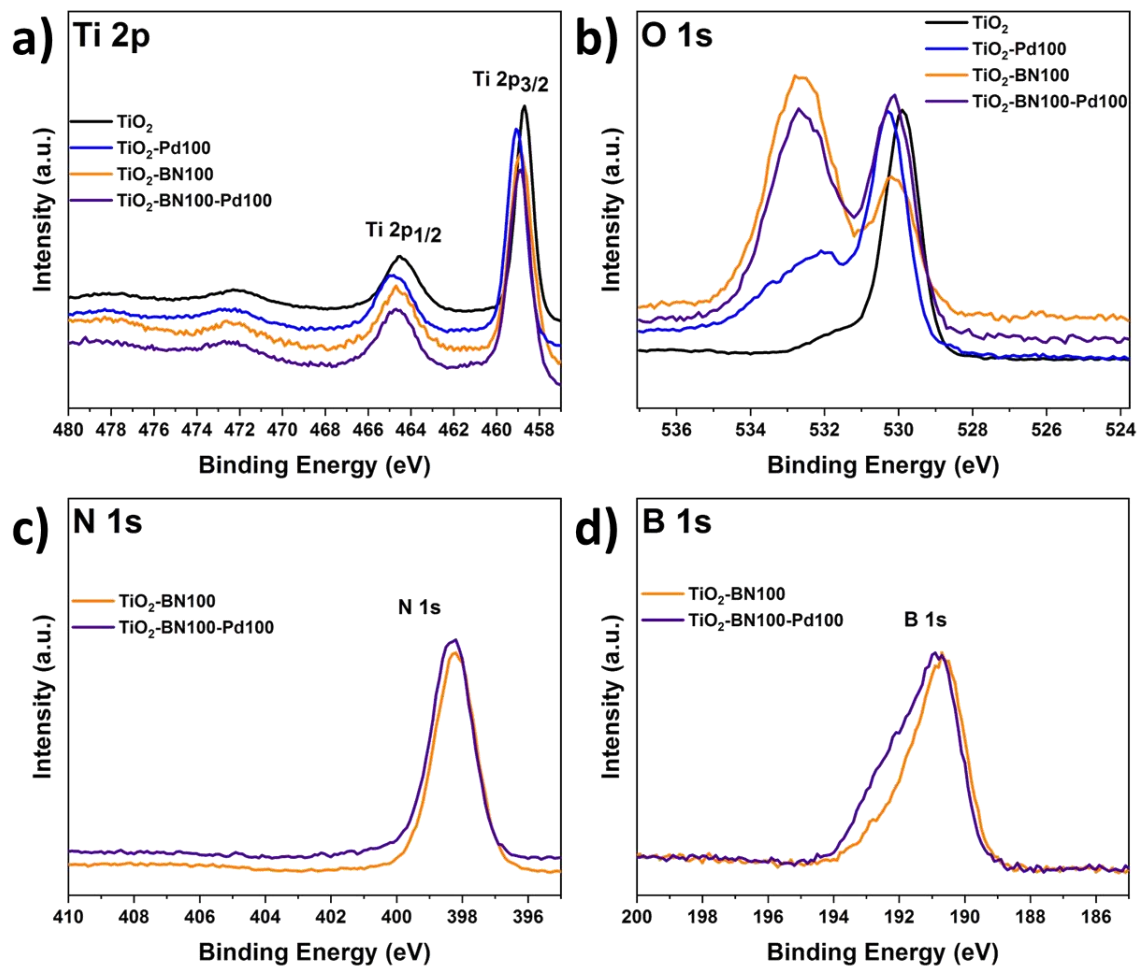


Figure 6: XPS data of a) Ti 2p b) O 1s c) N 1s and B 1s of all prepared samples.

As

shown

in

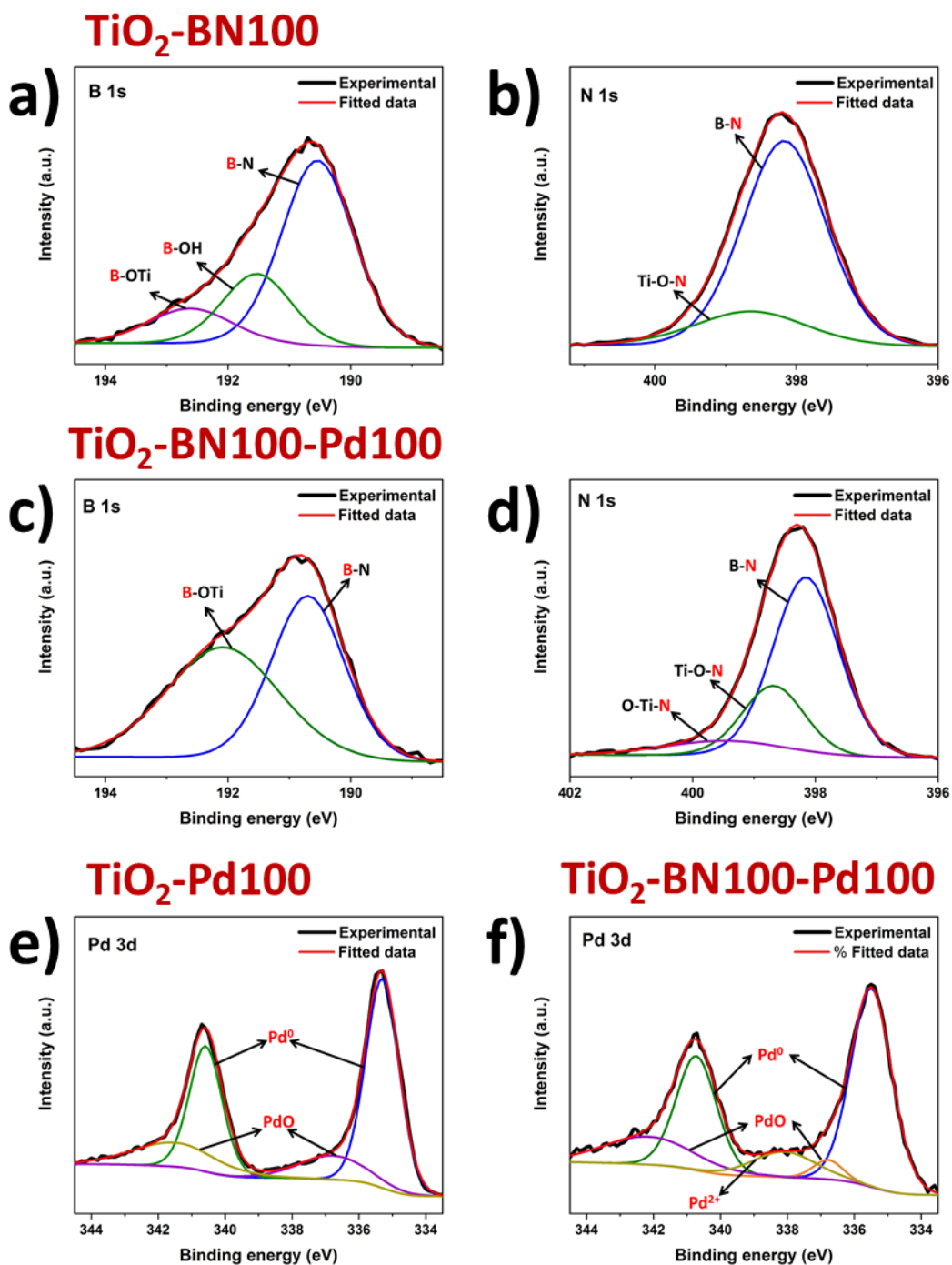


Figure 7a, the B 1s spectra consist of peaks at the binding energies of 190.5, 191.5 and 192.6 eV assigned to the edge or interfacial boron bonds connected with -N, -OH and -OTi, respectively. The presence of B-O-Ti bonds can also be proved by the O 1s spectra (Figure S5) which is

consigned to the formation of a chemical B-O-Ti bond between TiO_2 and boron at the edge of TiO_2 ⁴. For the TiO_2 -BN100-Pd100 sample, the B-OH peak was not noticeable due to the incorporation of Pd NPs on BN surface. In *Figure 7 b* the N 1s deconvolution peaks of TiO_2 -BN100 composite revealed the presence of two peaks with binding energy at 398.2 and 398.6 eV ascribed to B-N linkages with Ti-O and the presence of oxidized nitrogen such as N-O-Ti⁸⁸. The atomic percentage and binding energy of all the elements obtained by XPS are resumed in *Table S 1*.

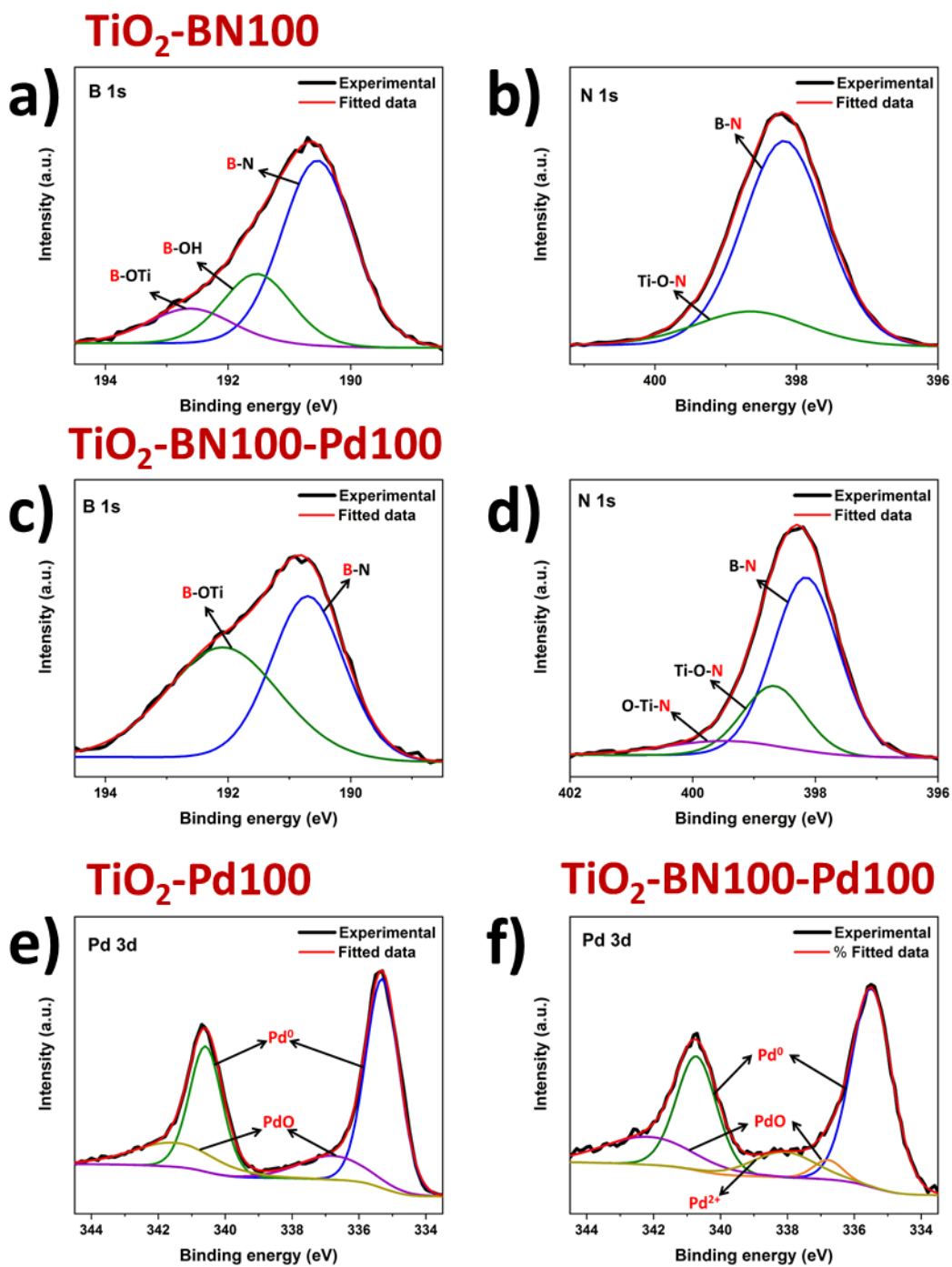


Figure 7: Deconvoluted XPS spectra of B 1s (a, c), N 1s (b,d) and Pd 3d (e,f) for modified TiO₂ by ALD.

Deconvolution of the XPS spectrum was performed to further understand the incorporation of Pd NPs in the prepared samples. From *Figure S2c*, two peaks at 335.5 and 340.6 eV assigned

to Pd 3d_{5/2} and Pd 3d_{3/2}.

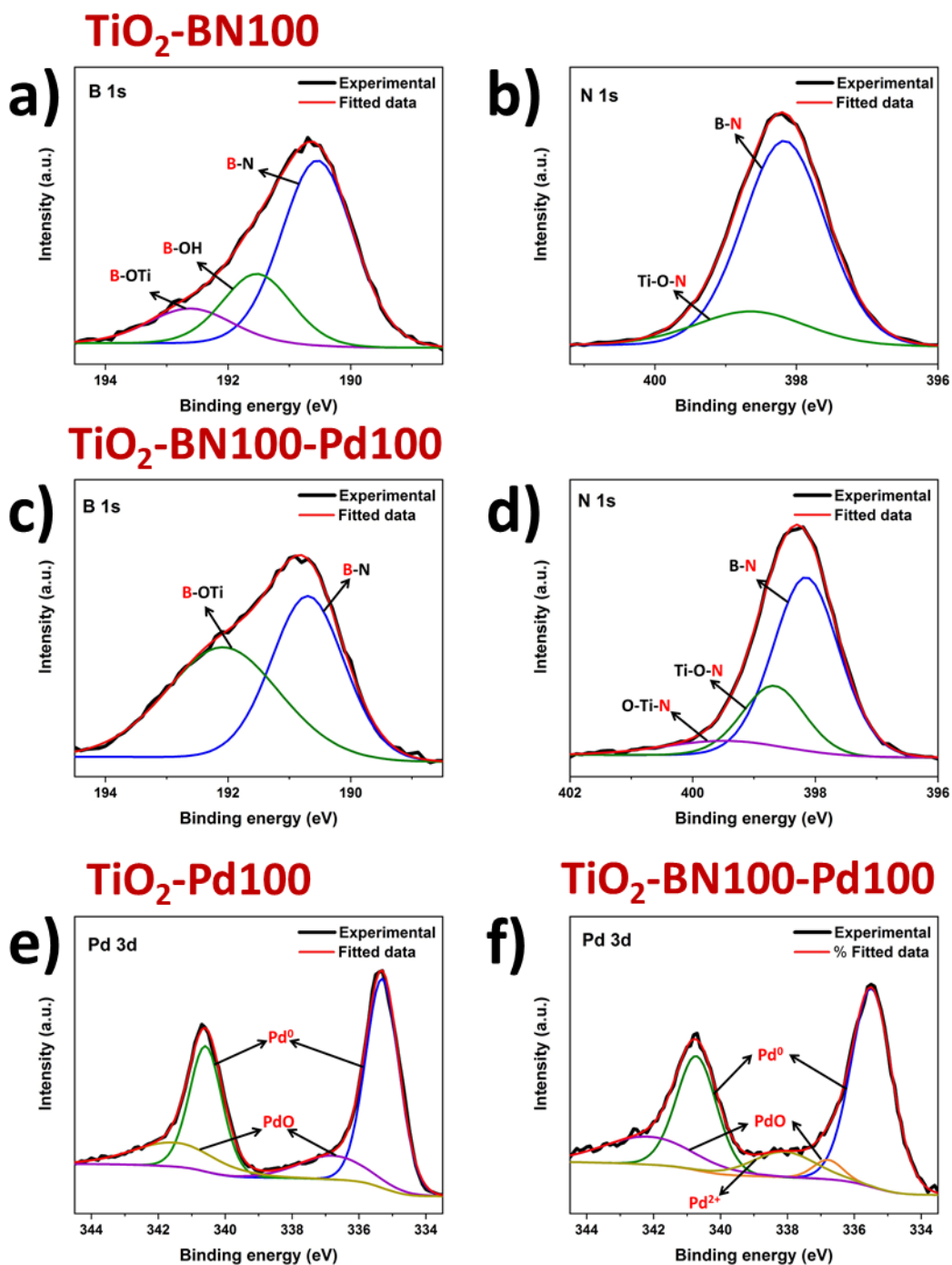


Figure 7 e-f shows a deconvoluted spectrum of Pd in sample TiO₂-Pd100 and TiO₂-BN100-Pd100, with the main species being Pd⁰ for all samples. Composite samples with BN and Pd shows an increase of oxidized Pd species, including PdO. This increase could be assigned to a higher Pd oxidation state on the sample's surface, even at low concentrations. Furthermore, the slight

increase of oxidized Pd species in the TiO₂-BN-Pd material in comparison with TiO₂-Pd might be explained by the fact that boron nitride attracts electrons from Pd⁸⁹.

The optical properties of pure TiO₂ NFs and TiO₂ composite nanofibers were obtained by UV-Vis absorption spectroscopy measurement. *Figure 8a* indicates that TiO₂ NFs absorbs light at 378 nm corresponding to a band gap of 3.2±0.01 eV. For TiO₂ nanocomposites fibers, the absorption edges are red-shifted with the energy of 3.17±0.02, 3.11±0.03, 3.11±0.02, 3.10±0.03 and 3.09 ±0.02, corresponding to TiO₂, TiO₂-Pd100, TiO₂-BN5, TiO₂-BN100, TiO₂-BN5-Pd and TiO₂-BN100-Pd, respectively. Moreover, all nanocomposite samples have another absorption edge in the visible range. The observed broad absorption peak was observed in the range of 400-580 nm, centered at 540-550nm. Decrease of the band gap value in TiO₂/BN samples has been reported previously¹⁰. The explanation of redshift of the band gap and increase of visible absorption in BN samples could be explained by forming new defect states at BN/TiO₂ interface. Formation of Pd-TiO₂ composite resulted in redshift of the band gap and increase of the visible absorption. It was shown that Pd²⁺ states transfer d-electrons towards TiO₂. Depending on electronic configurations (work functions, Fermi level position, ...) the d-electrons can reach for conductance band of TiO₂ or defect states⁹⁰.

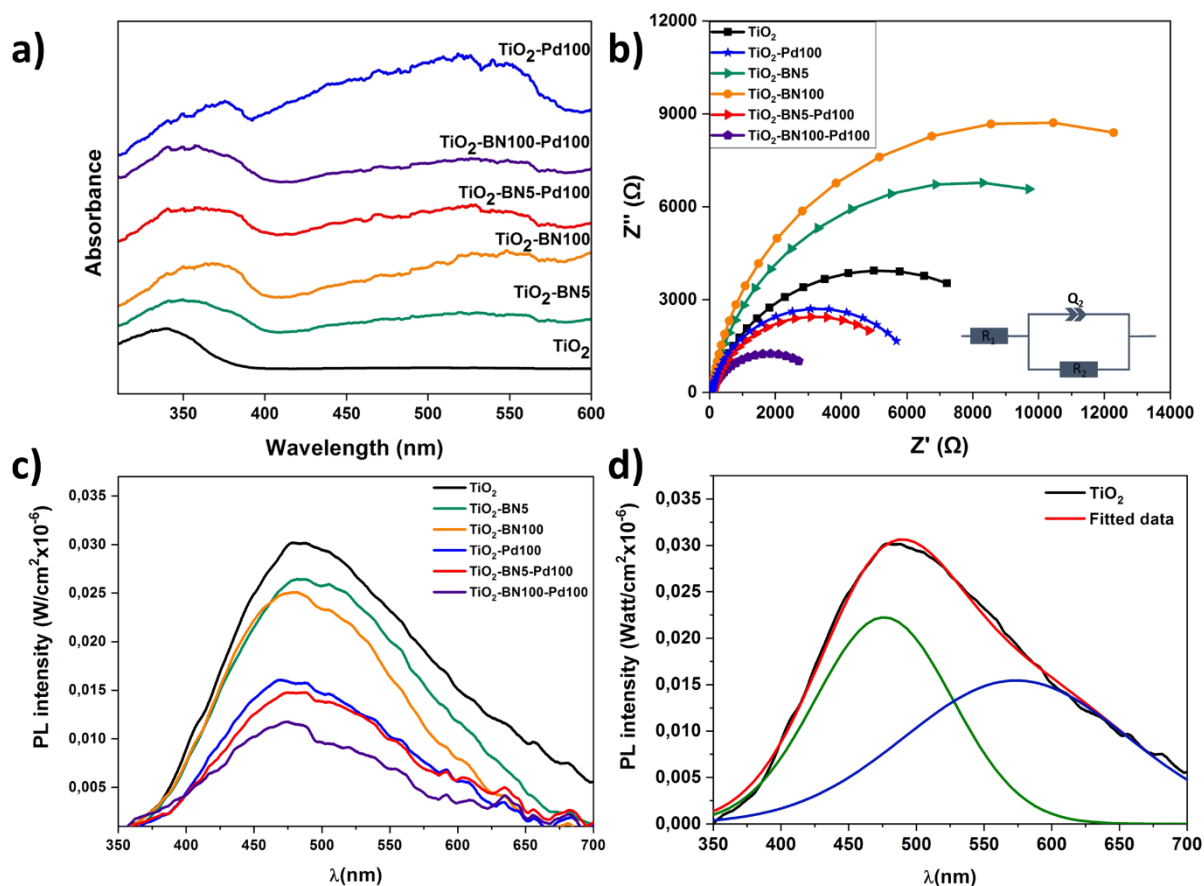


Figure 8. a) UV-Vis diffused reflectance of TiO₂ NFs and nanocomposites; b) EIS Nyquist plots of prepared nanofibers; c) Photoluminescence of all synthesized NFs; d) deconvolution of TiO₂ PL spectra

The PL spectra of the samples is shown in Figure 8c. Typically to TiO₂-based nanostructures, the intensity of the PL was low (quantum efficiency of TiO₂ ~0.005-0.01). All samples showed wide peak, centered at 480 nm. The wide peak of prepared TiO₂ nanostructures could be split into two peaks, located at 476 and 573 nm (Figure 8d). These peaks correspond to self-trapped excitons and oxygen vacancies, respectively^{17,91}. Modification of TiO₂ with Pd and BN nanostructures resulted in decreasing the PL. The lowest PL was observed for TiO₂-BN100-Pd100 pointing to higher charge separation rate. Photoluminescence of BN/TiO₂ was studied and explained by Nasr *et al.*¹⁰ Small concentrations of BN did not change PL, whereas high BN concentrations (5-10%) reduced PL intensity by 2 times. In addition, photoluminescence intensity decreased in samples with Pd due to formation of Schottky barrier between Pd and TiO₂⁹². Thus, Pd and BN act as

additional quenching factors of PL. Values of quantum efficiency test were presented in Table 1. It should be noted that the yields reported by others cannot be directly compared as there are differences in reactor systems, source of irradiation, volume and concentration of the catalyst⁹³. The apparent quantum yield is a parameter, which is usually defined as the ratio of converted reactant molecules over the number of photons entering the reactor. A metal oxide material such as TiO₂ (anatase and/or rutile) could never absorb all the incident photon flow from a given source, which can affect the calculation of QE⁹⁴. The values of absorption and scattering coefficients are represented in *Figure S4*. As shown in *Table 1*, higher quantum yield efficiency was attributed to TiO₂-BN-Pd nanocomposite, which the higher ACT degradation can explain.

Table 1: Anatase/ rutile faction, crystallite size, band gap and QE values of all catalysts.

Sample	Anatase (%)	Rutile (%)	Crystallite size (A) (nm)	Band gap (eV)	Quantum Efficiency (%)
TiO ₂	70.5	29.5	11.5	3.2±0.01	2.5
TiO ₂ -Pd100	67.1	32.9	11.6	3.17±0.02	3.6
TiO ₂ -BN5	53.7	46.2	23.5	3.11±0.03	0.9
TiO ₂ -BN100	43.6	56.4	32.4	3.11±0.02	1.3
TiO ₂ -BN5-Pd100	57.2	42.8	28.2	3.10±0.03	12.5
TiO ₂ -BN100-Pd100	53.4	46.6	35.3	3.09±0.02	21.7

The charge transfer resistance of the photogenerated carriers is investigated through EIS experiments. *Figure 8b* shows the Nyquist diagrams of pristine TiO₂ and modified TiO₂ samples. It was found that the diameters of the semicircle decreased with the doped samples with Pd or BN-Pd and the lower value was obtained with TiO₂-BN100-Pd100 nanocomposites. The smaller EIS radius demonstrates the weaker electronic impedance and higher separation of photogenerated electron-hole pairs. This phenomenon benefits from the electronic band structure formed when TiO₂ is doped with BN and Pd, and through this structure, the ultimate catalytic activities can be promoted. Moreover, Table 2 shows that the smallest polarization resistances are obtained on TiO₂-BN100-Pd100, where R1 represents the bulk resistance of electrodes and electrolyte, R2

denotes the resistance formed at the nanofibers' and electrolyte and Q2 designates the double layer capacitance at the nanofibers and the electrolyte interface. The lowest R_2 was attributed to TiO₂-BN100-Pd100 nanocomposites with a value of 3.74 K Ω , which refers to a lower resistance between fibers and electrolyte interface. TiO₂-BN100-Pd100 possesses a higher charge transfer rate and a better separation of photogenerated electron-hole than the other prepared catalysts, which is with good correlation with the degradation results.

Table 2. Resistance values from EIS of all synthesized nanofibers.

Sample	R_1 (Ω)	R_2 (K Ω)
TiO ₂	64.34	10.22
TiO ₂ -Pd100	65.56	6.44
TiO ₂ -BN5	76.88	15.86
TiO ₂ -BN100	83.17	19.82
TiO ₂ -BN5-Pd100	70.29	6.26
TiO ₂ -BN100-Pd100	63.66	3.74

3.2. PHOTOCATALYTIC DEGRADATION

In order to evaluate the modification of TiO₂ surface by ALD, photocatalytic performance of TiO₂ nanofibers with different amounts of Pd and BN were evaluated by degrading ACT in ultrapure water under UV and visible light. *Figure 9a-b* shows the degradation of ACT under UV light. Herein, the degradation rate was determined by LC-MS-MS every 5 minutes. It can be seen that the degradation with TiO₂-BN-Pd was faster than TiO₂. A total degradation of ACT was reached in less than 15 minutes with TiO₂-Pd100, TiO₂-BN5-Pd00 and TiO₂-BN100-Pd100 with a degradation rate of ACT corresponding to 0.06 mg.L⁻¹.min⁻¹ under UV irradiation. For TiO₂ catalyst, the process took 60 min until the degradation was complete. The fabrication of heterojunction with both BN and Pd at the same time has shown an efficient degradation under UV and visible light due to the enhancement of separation of electron-hole pairs as shown by PL and EIS results.

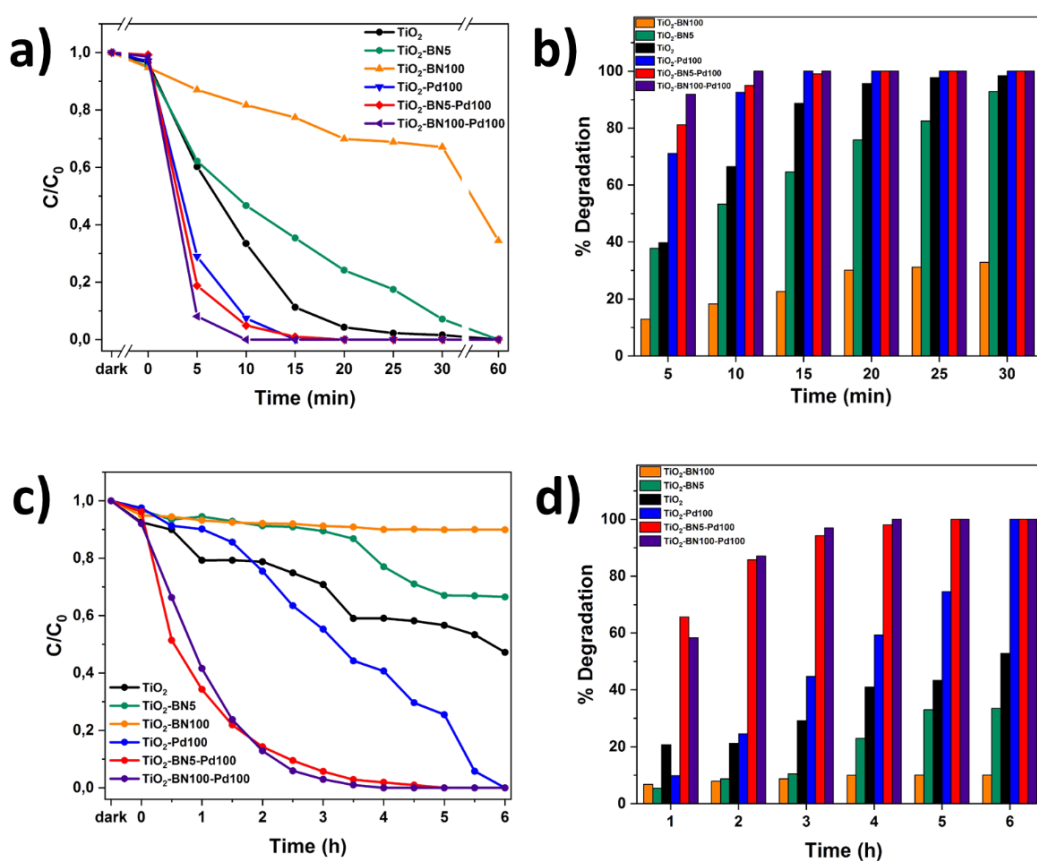


Figure 9. All prepared catalysts were decomposition of ACT and degradation percentage under a-b) UV and c-d) visible light irradiation. Each experiment was conducted for at least three times with relative errors of less than 5%.

After 30 min in the dark, the equilibrium was reached. *Figure 9a-c* shows that the degradation of ACT by $\text{TiO}_2\text{-BN-Pd}$ was faster than pristine TiO_2 . The degradation of the pollutant reached 87% with $\text{TiO}_2\text{-BN100-Pd100}$ after 2h of visible irradiation comparing to just 20% with TiO_2 not modified (*Figure 9b*). Furthermore, it can be clearly seen that when we add the Pd, the degradation efficiency increases, and after 4 hours of irradiation, 100% of the pollutant was degraded. The degradation speed of ACT using $\text{TiO}_2\text{-BN100-Pd100}$ under visible irradiation after 4 hours was $0.004 \text{ mg}\cdot\text{L}^{-1}\cdot\text{min}^{-1}$. This confirms that the Pd has shifted the band gap of TiO_2 to the visible range (confirmed by UV reflectance results), thus improving the catalytic activity under visible light⁴⁷. Moreover, *Figure 9d* showed that when using $\text{TiO}_2\text{-Pd100}$ as a photocatalyst, the degradation has slightly improved compared to TiO_2 after 2 hours. A degradation percentage of

24% versus 21% was obtained. After 6 hours, the nanocomposite has led to a total degradation of ACT in comparison with pure TiO_2 that had degraded only 50% of the pollutant. Doping with noble metals like Pd is an effective method to improve the photocatalytic efficiency of TiO_2 as this increases its visible-light capacity. When comparing TiO_2 -BN-Pd nanocomposites and TiO_2 -Pd, degradation of ACT was enhanced with TiO_2 -BN-Pd. Shing *et al.* have already confirmed that heterojunction engineering promoted charge transfer and enhanced photocatalytic activities of photocatalysts⁹⁵. This could be explained by the formation of Schottky junctions at the interface of noble metal nanoparticles and the semiconductor. The addition of Pd nanoparticles onto TiO_2 -BN surface improves UV-Visible light degradation of TiO_2 and creates Schottky junctions, which reduces the recombination of photogenerated carriers in TiO_2 ⁹⁶. Moreover, TiO_2 -BN100-Pd100 showed a better degradation efficiency than TiO_2 -BN5-Pd100 and this is due to the lower amount of Pd deposited on TiO_2 -BN100 as confirmed by TEM images. It was found that excessive Pd loading could decrease the performance of the catalyst. Moreover, Leong *et al.* demonstrated that the synergistic effects of the $-\text{O}-\text{Pd}-\text{O}-$ surface species are mainly responsible for the enhanced photocatalytic activity, which confirms our findings since TiO_2 -BN100-Pd100 possesses a higher % of Pd-O than TiO_2 -BN5-Pd100 confirmed by deconvoluted XPS data⁹⁷.

The kinetic behavior of the as-prepared catalysts was also investigated under both lights. The photodegradation reactions follow a pseudo-first-order reaction³³.

Figure 10a-c shows the linear dependence between $\ln(C_0/C)$ and time. The degradation rate increased as follow: TiO_2 -BN100 < TiO_2 -BN5 < TiO_2 < TiO_2 -Pd100 < TiO_2 -BN5-Pd100 < TiO_2 -BN100-Pd100 under visible light as shown in

Figure 10b. The degradation rate of TiO_2 -BN100-Pd100 nanocomposite is 9 time higher than TiO_2 nanofibers under visible light and almost 2 times higher under UV light. These results confirm the role of heterojunction between TiO_2 , BN and Pd in enhancing the degradation of ACT under visible light. Palladium decreases the band gap of TiO_2 , as confirmed by UV reflectance and photoluminescence results, leading to a higher degradation in the visible range, while BN improves the separation efficiency of electron – holes (confirmed by PL results). The increase of photocatalytic degradation of ACT in the presence of BN and Pd could be attributed to the fast

transfer of photogenerated electrons from the semiconductor (BN) to the metal NPs (Pd), which enhances the separation of the electrons and holes. Moreover, the shift in optical absorption of the catalyst in the visible region is attributed to the Pd loading and the formation of B-O-Ti bond. This leads to an energy rearrangement that will affect the charge balance. Hence, the band gap of TiO₂-BN-Pd is narrowed and excited wavelength is extended from UV to visible light region^{44,97,98}.

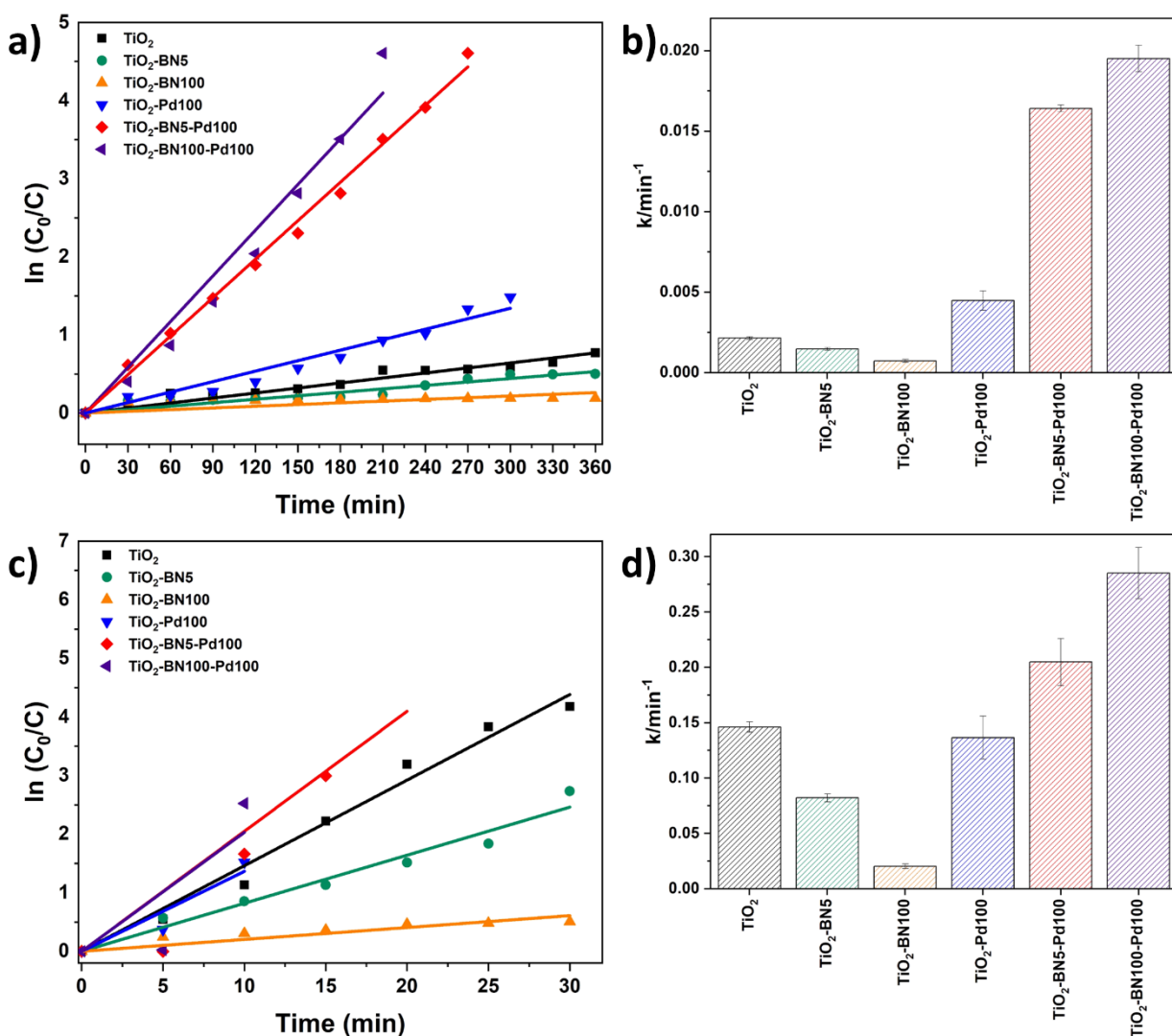


Figure 10. Kinetics models and rate constant values of ACT degradation under a-b) UV and c-d) visible irradiation, respectively. All experiments were conducted for at least three times and relative errors were less than 5%.

Since TiO₂-BN100-Pd100 nanocomposites has shown the best degradation efficiency, a stability test was performed to confirm the reusability of the catalyst. After each cycle, the catalyst was filtered, washed with deionized water, dried at 100°C then reused with no further steps. In

Figure 11a, the degradation of ACT remained unchanged under visible light after 5 cycles. For UV irradiation, the degradation efficiency dropped by less than 5% after the second cycle, but kept almost stable until the fifth cycle (

Figure 11b). This reveals that using ALD allows maximising the metal-support interaction, increasing the active sites, and improving the catalyst's stability. The prepared catalyst remains stable and can be reused to degrade water pollutants, thus aiming at the advantage of atomic layer deposition in the photocatalytic field.

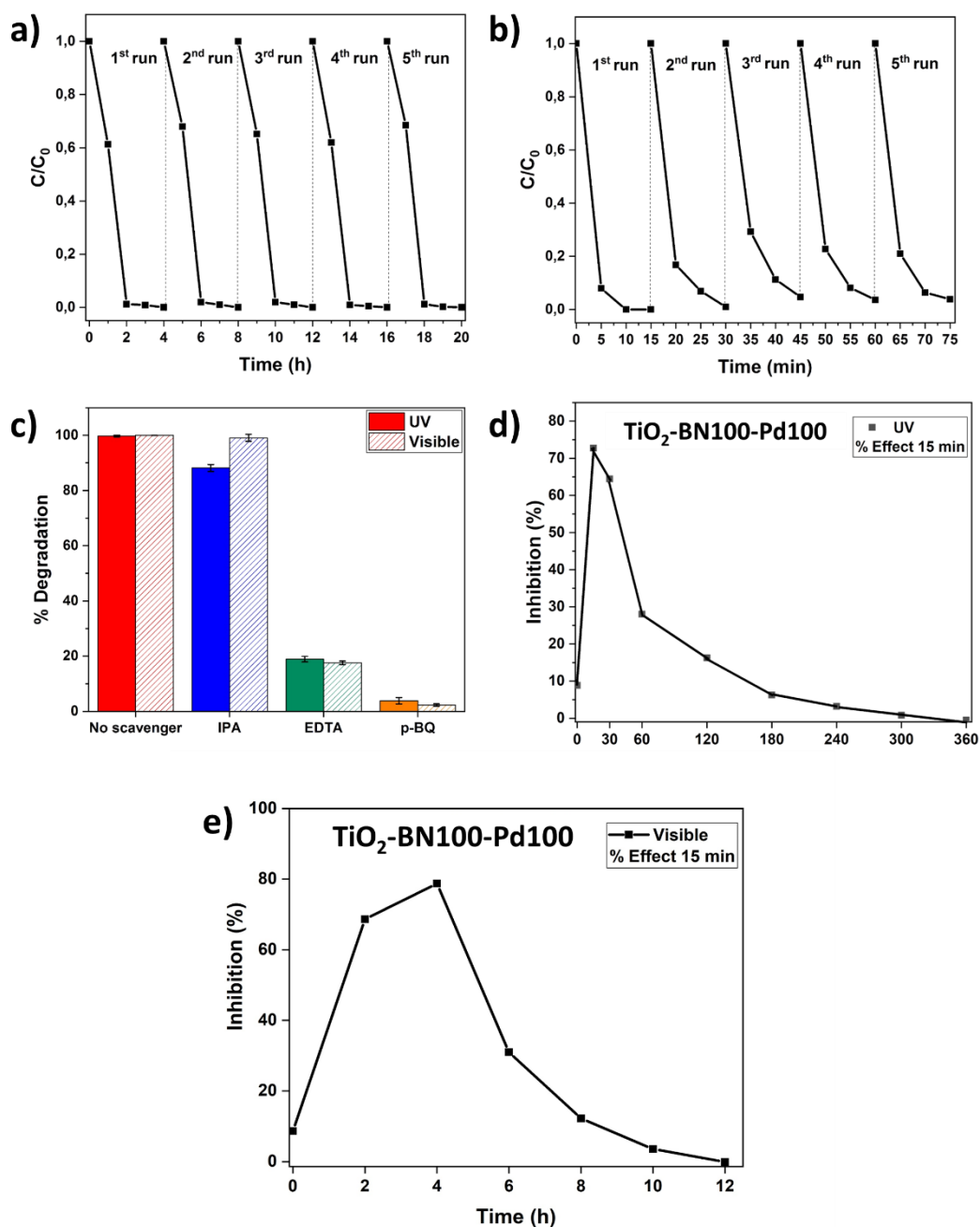


Figure 11. Recycling test of $\text{TiO}_2\text{-BN100-Pd100}$ under a) visible and b) UV irradiation; c) Scavenger plot for determining reactive species in the degradation of ACT by $\text{TiO}_2\text{-BN100-Pd100}$; Inhibition of luminescence of *V. fischeri* marine bacteria during ACT photocatalysis after 15min exposure between the bacterial strain and the degradation solution d) under UV irradiation and e) under visible irradiation.

All further tests were done on TiO₂-BN100-Pd100 nanocomposites. It is known that three main active species could participate in the catalytic process. In order to understand the mechanism of the degradation of ACT by the catalyst, trapping experiments were carried out. Ethylenediaminetetracetate (EDTA), p-benzoquinone (p-BQ) and isopropanol (IPA) were used as trapping reagents for holes (h^+), superoxide radicals ($\cdot O_2^-$) and hydroxyl radicals ($\cdot OH$), respectively.

Figure 11c shows that the degradation efficiency has clearly decreased from 100% to less than 20% when adding p-BQ and EDTA, while it remains almost unchanged when adding IPA under both lights UV and Visible, showing that $\cdot OH$ do not contribute in the degradation. However, $\cdot O_2^-$ and h^+ , both has a major role in the photocatalytic degradation of ACT.

3.3. Toxicity tests

Identification of ACT intermediates and their metabolic pathways is essential to evaluate their potential impacts on human health, the environment and other aquatic life forms. In this work, we found that $\cdot O_2^-$ and h^+ are the active species in the photocatalytic degradation of ACT, this agrees with previously published results⁹⁹. Zhang *et al.* suggested a direct hole (h^+) oxidation route as the initial step for ACT degradation. Then the formed phenolic radical loses a cation and leads to phenoxyl radicals that will react with superoxide radical. During this route, harmful metabolites could be formed. Some of these intermediates could be more harmful than the initial pollutant, such as 1,4-benzoquinone, benzoic acid and benzaldehyde. In order to understand the pathways degradation, the global toxicity of the solution was studied. ACT itself shows a low inhibition percentage (8%) as it is not a hazardous pollutant for this strain of bacteria (

Figure 11 c-d). After 15 min time contact between the solution and *V. fischeri* bacteria, the acute toxicity of the treated solution strain increased rapidly at the early stage of the treatment and reached 68% at 15 min UV irradiation (Figure 11 c) and 72% after 2h visible irradiation (Figure 11 d). This result is relevant and consistent with regard to the previously proved formation of toxic aromatic by-products such as 1,4-benzoquinone, benzoic acid and benzaldehyde⁷⁴⁻⁷⁶. After 3h UV

irradiation and 12h degradation under visible light, the toxicity markedly declined to a value near 0% inhibition and lower than the initial % of inhibition of ACT. At that point, short-chain carboxylic acids and aromatic compounds could be formed continuously and then transformed to none toxic compounds. Further studies should be done to identify all the byproductsof this degradation mechanism. As mentioned before, the photocatalyst used in this work was not reported before, but a comparison with other works was summarized in *Table 3*. The comparison is not easy since many factors could vary such as pollutant concentration, catalyst concentration, pH of the solution and most importantly the irradiation type. However, it can be clearly seen that the prepared catalyst (TiO₂-BN-Pd) showed interesting results with a high degradation efficiency, recyclability, and most importantly, fast degradation rate.

Table 3: Comparison of degradation efficiency of differently prepared photocatalysts

Pollutant	C _{Pollutant} (mg.L ⁻¹)	Photocatalyst	C _{Catalyst} (g.L ⁻¹)	Type of irradiation	Energy (W.m ⁻²)	Degradation time (min)	pH	Removal efficiency (%)	References
ACT	1	TiO ₂ -BN100-Pd100	0.5	Medium pressure metal halide UV	NA	10	6.8	100	In this work
ACT	1	TiO ₂ -BN100-Pd100	0.5	halogen linear lamp	NA	180	6.8	98	In this work
ACT	20	Pt-TiO ₂	0.4	Solar irradiation	500	180	6.3	100	103
ACT	20	Degussa P25	2	UV irradiation 365nm	NA	60	NA	98	104
ACT	0.08	TiO ₂ -Ag5%	1	UV irradiation 365nm	NA	180	NA	98	105
ACT	15	K ₂ S ₂ O ₈ -TiO ₂	2	Visible irradiation LED lamps	168.5	390	6.9	93	106
MO	10	10%BN/TiO ₂ NFs	0.4	UV irradiation	NA	75	NA	99	10
MB	10	BN/TiO ₂ composite	0.33	Visible light	NA	200	NA	79	4

RhB	10	12 wt% BN/TiO ₂	0.5	visible-light Xe lamp	1000	150	NA	99	107
ACT	10	MWCNT10%-TiO ₂ -SiO ₂	NA	Visible irradiation high pressure mercury lamp	73.1–75.3	60	7	81.6	108
ACT	30	Fe ₂ O ₃ -TiO ₂	0.25	solar simulator halogen lamp	140	180	8	94.8	109
ACT	5	BaTiO ₃ /TiO ₂ (3 :1)	1	UV/Vis xenon lamp	NA	240	7	95	110
ACT	50	TiO ₂ @rGO TG ₃	2	UVA/LED	950	50	5.4	100	111
RhB	10	12% h-BN/TiO ₂	0.75	visible light	NA	120	NA	95	11
ACT	5	3% (w/w) WO ₃ /TiO ₂ /SiO ₂	1.5	xenon lamp	NA	360	9	95	112
ACT	18	TiO ₂ -NFs-SSF	NA	UV light Blue lamps	27	200	6-7	40	113
MB	2	5%Pd/TiO ₂	NA	visible white light	4	1500	NA	10	98
AMX	20	Pd/TiO ₂	4	Visible light tungsten	NA	300	NA	97.5	97

4. Conclusion

To sum up, by combining two different techniques, electrospinning and ALD, six photocatalysts based on TiO₂ nanofibers coated by BN and Pd by ALD were synthesized: pristine

TiO₂, TiO₂-Pd100, TiO₂-BN5, TiO₂-BN100, TiO₂-BN5-Pd100 and TiO₂-BN100-Pd100. The influence of nanocomposites catalyst on degradation of water pollutants was studied, using ACT as a model pollutant. XRD and RAMAN spectroscopy results indicate that the modification mechanism by ALD, allowed the combination of crystalline phases of TiO₂ with different percentages of anatase-rutile phase. Moreover, TEM images showed the good dispersion of Pd NPs on the surface of nanofibers, the amount of Pd decreased with the increase of BN cycles. TiO₂/BN/Pd samples showed the best photocatalytic activity regarding ACT visible light irradiation (9 times higher than bare TiO₂), though their efficiency depends on the Schottky barrier-type separation from the deposition of another heterojunction material and noble metals on TiO₂. PL and EIS results confirmed that TiO₂-BN-Pd hybrids own a superior charge separation ability from TiO₂, TiO₂-BN and TiO₂-Pd, which was devoted in the higher degradation efficiency. Finally, the use of the ALD technique to modify the interface of TiO₂ shows a very promising pathway to enhance degradation of micropollutant and their intermediates in wastewater, by allowing a conformal coating with thickness control and formation of composites materials. Although additional studies should be conducted with other pollutants and on wastewater to estimate the real efficiency of the prepared nanomaterials, the results presents open prospects for the tuning of photocatalysts by ALD.

Acknowledgments

This study was financially supported by the French National Agency (ANR, program MeNiNA-ANR-17-CE09-0049). The authors thank Bruno Navarra (CNRS-IEM) for his technical assistance on ALD. The authors would also like to acknowledge Valérie Flaud (ICGM, France) for XPS technical support. I.I. acknowledges the partial financial support from the National Science Centre (NCN) of Poland by the SONATA-BIS grant 2020/38/E/ST5/00176.

References

1. Mekonnen MM, Hoekstra AY. Four billion people facing severe water scarcity. *Sci Adv.* 2016;2(2):e1500323.

2. Gopinath KP, Madhav NV, Krishnan A, Malolan R, Rangarajan G. Present applications of titanium dioxide for the photocatalytic removal of pollutants from water: A review. *J Environ Manage*. 2020;270:110906. doi:10.1016/j.jenvman.2020.110906
3. Hou C, Jiao T, Xing R, Chen Y, Zhou J, Zhang L. Preparation of TiO₂ nanoparticles modified electrospun nanocomposite membranes toward efficient dye degradation for wastewater treatment. *J Taiwan Inst Chem Eng*. 2017;78:118-126. doi:10.1016/j.jtice.2017.04.033
4. Singh B, kaur G, Singh P, et al. Nanostructured BN–TiO₂ composite with ultra-high photocatalytic activity. *New J Chem*. 2017;41(20):11640-11646. doi:10.1039/C7NJ02509B
5. Van Doorslaer X, Dewulf J, De Maerschalk J, Van Langenhove H, Demeestere K. Heterogeneous photocatalysis of moxifloxacin in hospital effluent: Effect of selected matrix constituents. *Photocatal Disinfect Remov Contam Emerg Concern*. 2015;261:9-16. doi:10.1016/j.cej.2014.06.079
6. Nada AA, Orimolade BO, El-Maghrabi HH, et al. Photoelectrocatalysis of paracetamol on Pd–ZnO/N-doped carbon nanofibers electrode. *Appl Mater Today*. 2021;24:101129.
7. Titchou FE, Zazou H, Afanga H, et al. Electrochemical oxidation treatment of Direct Red 23 aqueous solutions: Influence of the operating conditions. *Sep Sci Technol*. Published online September 26, 2021:1-20. doi:10.1080/01496395.2021.1982978
8. Zhang J, Hou X, Pang Z, et al. Author 's Accepted Manuscript Fabrication of hierarchical TiO₂ nanofibers by microemulsion electrospinning for photocatalysis applications. *Ceram Int*. Published online 2017. doi:10.1016/j.ceramint.2017.08.166
9. Stucchi M, Bianchi CL, Argirusis C, et al. Ultrasound assisted synthesis of Ag-decorated TiO₂ active in visible light. *Ultrason Sonochem*. 2018;40:282-288. doi:10.1016/j.ultsonch.2017.07.016
10. Nasr M, Viter R, Eid C, Habchi R, Miele P, Bechelany M. Enhanced photocatalytic performance of novel electrospun BN/TiO₂ composite nanofibers. *New J Chem*. 2017;41(1):81-89. doi:10.1039/C6NJ03088B
11. Li Q, Hou X, Fang Z, et al. Construction of layered h-BN/TiO₂ hetero-structure and probing of the synergetic photocatalytic effect. *Sci China Mater*. 2020;63(2):276-287. doi:10.1007/s40843-019-1180-8
12. García-Zaleta DS, Torres-Huerta AM, Domínguez-Crespo MA, García-Murillo A, Silva-Rodrigo R, González RL. Influence of Phases Content on Pt/TiO₂, Pd/TiO₂ Catalysts for Degradation of 4-Chlorophenol at Room Temperature. Low J, ed. *J Nanomater*. 2016;2016:1805169. doi:10.1155/2016/1805169

13. Wang M, Liu Z, Fang M, et al. Enhancement in the photocatalytic activity of TiO₂ nano fibers hybridized with g-C₃N₄ via electrospinning. 2016;55:2-8. doi:10.1016/j.solidstatesciences.2016.02.002
14. Zhou C, Lai C, Zhang C, et al. Semiconductor/boron nitride composites: Synthesis, properties, and photocatalysis applications. *Appl Catal B Environ*. 2018;238:6-18. doi:10.1016/j.apcatb.2018.07.011
15. Ramanavicius S, Ramanavicius A. Insights in the Application of Stoichiometric and Non-Stoichiometric Titanium Oxides for the Design of Sensors for the Determination of Gases and VOCs (TiO_{2-x} and TiO_{2n-1} vs. TiO₂). *Sensors*. 2020;20(23). doi:10.3390/s20236833
16. Ramanavicius S, Tereshchenko A, Karpicz R, et al. TiO_{2-x}/TiO₂-structure based 'self-heated' sensor for the determination of some reducing gases. *Sensors*. 2020;20(1):74.
17. Nasr M, Abou Chaaya A, Abboud N, et al. Photoluminescence: A very sensitive tool to detect the presence of anatase in rutile phase electrospun TiO₂ nanofibers. *Superlattices Microstruct*. 2015;77:18-24. doi:10.1016/j.spmi.2014.10.034
18. Sayed Farheen N, Jayakumar OD, Sasikala R, et al. Photochemical Hydrogen Generation Using Nitrogen-Doped TiO₂-Pd Nanoparticles: Facile Synthesis and Effect of Ti³⁺ Incorporation. *J Phys Chem C*. 2012;116(23):12462-12467. doi:10.1021/jp3029962
19. Nasr M, Balme S, Eid C, Habchi R, Miele P, Bechelany M. Enhanced Visible-Light Photocatalytic Performance of Electrospun rGO/TiO₂ Composite Nanofibers. *J Phys Chem C*. 2017;121(1):261-269. doi:10.1021/acs.jpcc.6b08840
20. Khan H, Jiang Z, Berk D. Molybdenum doped graphene/TiO₂ hybrid photocatalyst for UV/visible photocatalytic applications. *Sol Energy*. 2018;162:420-430. doi:10.1016/j.solener.2018.01.055
21. Pascariu P, Airinei A, Iacomi F, Bucur S, Sucheai MP. Chapter 12 - Electrospun TiO₂-based nanofiber composites and their bio-related and environmental applications. In: Dinca V, Sucheai MP, eds. *Functional Nanostructured Interfaces for Environmental and Biomedical Applications*. Elsevier; 2019:307-321. doi:10.1016/B978-0-12-814401-5.00012-8
22. Chen Z, Zhao J, Yang X, et al. Fabrication of TiO₂/WO₃ Composite Nanofibers by Electrospinning and Photocatalytic Performance of the Resultant Fabrics. *Ind Eng Chem Res*. 2016;55(1):80-85. doi:10.1021/acs.iecr.5b03578
23. Shanmugam V, Sanjeevamuthu S, Jeyaperumal KS, Vairamuthu R. Fabrication of heterostructured vanadium modified g-C₃N₄/TiO₂ hybrid photocatalyst for improved photocatalytic performance under visible light exposure and antibacterial activities. *J Ind Eng Chem*. 2019;76:318-332. doi:10.1016/j.jiec.2019.03.056

24. Lin L, Wang H, Xu P. Immobilized TiO₂-reduced graphene oxide nanocomposites on optical fibers as high performance photocatalysts for degradation of pharmaceuticals. *Chem Eng J*. Published online 2017. doi:10.1016/j.cej.2016.04.024
25. Tao W, Wang M, Ali R, et al. Multi-layered porous hierarchical TiO₂/g-C₃N₄ hybrid coating for enhanced visible light photocatalysis. *Appl Surf Sci*. 2019;495:143435. doi:10.1016/j.apsusc.2019.07.177
26. Barhoum A, El-Maghrabi HH, Iatsunskiy I, et al. Atomic layer deposition of Pd nanoparticles on self-supported carbon-Ni/NiO-Pd nanofiber electrodes for electrochemical hydrogen and oxygen evolution reactions. *J Colloid Interface Sci*. 2020;569:286-297. doi:10.1016/j.jcis.2020.02.063
27. Khojasteh H, Salavati-niasari M, Sadat F. Photocatalytic evaluation of RGO / TiO₂ NWs / Pd-Ag nanocomposite as an improved catalyst for efficient dye degradation. 2018;746:611–618. doi:10.1016/j.jallcom.2018.02.345
28. Zhu Y, Gao C, Bai S, et al. Hydriding Pd cocatalysts: An approach to giant enhancement on photocatalytic CO₂ reduction into CH₄. *Nano Res*. 2017;10:1-11. doi:10.1007/s12274-017-1552-0
29. Duan H, Wang Z, Cui L, Lin B, Zhou Y. Stability Investigation of a Supported TiO₂-Pd Bifunctional Catalyst over the One-Pot Liquid-Phase Synthesis of Methyl Isobutyl Ketone from Acetone and H₂. *Ind Eng Chem Res*. 2018;57(37):12358-12366. doi:10.1021/acs.iecr.8b02854
30. Espino-Estévez MR, Fernández-Rodríguez C, González-Díaz OM, et al. Effect of TiO₂-Pd and TiO₂-Ag on the photocatalytic oxidation of diclofenac, isoproturon and phenol. *Chem Eng J*. 2016;298:82-95. doi:10.1016/j.cej.2016.04.016
31. Meng A, Zhang L, Cheng B, Yu J. Dual Cocatalysts in TiO₂ Photocatalysis. 2019;1807660:1-31. doi:10.1002/adma.201807660
32. Jiang G, Geng K, Wu Y, Han Y, Shen X. High photocatalytic performance of ruthenium complexes sensitizing g-C₃N₄/TiO₂ hybrid in visible light irradiation. *Appl Catal B Environ*. 2018;227:366-375. doi:10.1016/j.apcatb.2018.01.034
33. Nasr M, Soussan L, Viter R, et al. High photodegradation and antibacterial activity of BN-Ag/TiO₂ composite nanofibers under visible light. *New J Chem*. 2018;42(2):1250-1259. doi:10.1039/C7NJ03183A
34. Lee Cgyu, Na K han, Kim W tae, Park D cheol, Yang W hee, Choi W youl. applied sciences TiO₂ / ZnO Nanofibers Prepared by Electrospinning and Their Photocatalytic Degradation of Methylene Blue Compared with TiO₂ Nanofibers. Published online 2019.

35. Park SM, Razzaq A, Park YH, et al. Hybrid $\text{Cu}_2\text{O}-\text{TiO}_2$ Heterostructured Composites for Photocatalytic CO_2 Reduction into Methane Using Solar Irradiation: Sunlight into Fuel. *ACS Omega*. 2016;1(5):868-875. doi:10.1021/acsomega.6b00164
36. Peng C, Yang X, Li Y, Yu H, Wang H, Peng F. Hybrids of Two-Dimensional Ti_3C_2 and TiO_2 Exposing {001} Facets toward Enhanced Photocatalytic Activity. *ACS Appl Mater Interfaces*. 2016;8(9):6051-6060. doi:10.1021/acsami.5b11973
37. Coy E, Siuzdak K, Grądzka-Kurzej I, et al. Exploring the effect of BN and BN bridges on the photocatalytic performance of semiconductor heterojunctions: Enhancing carrier transfer mechanism. *Appl Mater Today*. 2021;24:101095.
38. Bechelany M, Brioude A, Stadelmann P, Bernard S, Cornu D, Miele P. Preparation of BN Microtubes/Nanotubes with a Unique Chemical Process. *J Phys Chem C*. 2008;112(47):18325-18330. doi:10.1021/jp804286x
39. Gao X, Yao Y, Meng X. Recent development on BN-based photocatalysis: A review. *Mater Sci Semicond Process*. 2020;120:105256. doi:10.1016/j.mssp.2020.105256
40. Lin L, Lin L, Jiang W, Bechelany M, Nasr M, Jarvis J. Adsorption and photocatalytic oxidation of ibuprofen using nanocomposites of TiO_2 nanofibers combined with BN nanosheets : Degradation products and mechanisms Chemosphere Adsorption and photocatalytic oxidation of ibuprofen using nanocomposites of TiO_2 n. *Chemosphere*. 2019;220(December 2018):921-929. doi:10.1016/j.chemosphere.2018.12.184
41. Sheng Y, Yang J, Wang F, et al. Sol-gel synthesized hexagonal boron nitride/titania nanocomposites with enhanced photocatalytic activity. *Appl Surf Sci*. 2019;465:154-163. doi:10.1016/j.apsusc.2018.09.137
42. Li Z, Meng X. Recent development on palladium enhanced photocatalytic activity: A review. *J Alloys Compd*. 2020;830:154669. doi:10.1016/j.jallcom.2020.154669
43. Coy E, Siuzdak K, Pavlenko M, et al. Enhancing photocatalytic performance and solar absorption by schottky nanodiodes heterojunctions in mechanically resilient palladium coated TiO_2/Si nanopillars by atomic layer deposition. *Chem Eng J*. 2020;392:123702. doi:https://doi.org/10.1016/j.cej.2019.123702
44. Linic S, Aslam U, Boerigter C, Morabito M. Photochemical transformations on plasmonic metal nanoparticles. *Nat Mater*. 2015;14(6):567-576. doi:10.1038/nmat4281
45. Mohapatra SK, Kondamudi N, Banerjee S, Misra M. Functionalization of Self-Organized TiO_2 Nanotubes with Pd Nanoparticles for Photocatalytic Decomposition of Dyes under Solar Light Illumination. *Langmuir*. 2008;24(19):11276-11281. doi:10.1021/la801253f

46. Wu Z, Sheng Z, Liu Y, Wang H, Tang N, Wang J. Characterization and activity of Pd-modified TiO₂ catalysts for photocatalytic oxidation of NO in gas phase. *J Hazard Mater.* 2009;164(2):542-548. doi:10.1016/j.jhazmat.2008.08.028
47. Rusinque B, Lasa H. Photoreduction of a Pd-Doped Mesoporous TiO₂ Photocatalyst for Hydrogen Production under Visible Light. *Catalysts.* 2020;10:74. doi:10.3390/catal10010074
48. Drunka R, Grabis J, Krūmiņa A. Preparation of Au, Pt, Pd and Ag Doped TiO₂ Nanofibers and their Photocatalytic Properties under LED Illumination. *Key Eng Mater.* 2018;762:283-287. doi:10.4028/www.scientific.net/KEM.762.283
49. Tang Q, Meng X, Wang Z, Zhou J, Tang H. One-step Electrospinning Synthesis of TiO₂ / g-C₃N₄ Nanofibers with Enhanced Photocatalytic Properties. *Appl Surf Sci.* Published online 2017. doi:10.1016/j.apsusc.2017.07.288
50. Weber M, Julbe A, Ayrál A, Miele P, Bechelany M. Atomic Layer Deposition for Membranes: Basics, Challenges, and Opportunities. *Chem Mater.* 2018;30(21):7368-7390. doi:10.1021/acs.chemmater.8b02687
51. Graniel O, Weber M, Balme S, Miele P, Bechelany M. Atomic layer deposition for biosensing applications. *Biosens Bioelectron.* 2018;122:147-159. doi:https://doi.org/10.1016/j.bios.2018.09.038
52. Mackus AJM, Weber MJ, Thissen NFW, et al. Atomic layer deposition of Pd and Pt nanoparticles for catalysis: on the mechanisms of nanoparticle formation. *Nanotechnology.* 2015;27(3):034001. doi:10.1088/0957-4484/27/3/034001
53. Najem M, Nada AA, Weber M, et al. Palladium/Carbon Nanofibers by Combining Atomic Layer Deposition and Electrospinning for Organic Pollutant Degradation. *Materials.* 2020;13(8). doi:10.3390/ma13081947
54. Weber M, Bechelany M. Combining nanoparticles grown by ALD and MOFs for gas separation and catalysis applications. *Pure Appl Chem.* 2019;92. doi:10.1515/pac-2019-0109
55. Ramachandran RK, Detavernier C, Dendooven J. Atomic Layer Deposition for Catalysis. In: *Nanotechnology in Catalysis.* John Wiley & Sons, Ltd; 2017:335-358. doi:10.1002/9783527699827.ch14
56. George SM. Atomic Layer Deposition: An Overview. *Chem Rev.* 2010;110(1):111-131. doi:10.1021/cr900056b
57. Weber M, Verheijen M, Bol A, Kessels W. Sub-nanometer dimensions control of core/shell nanoparticles prepared by atomic layer deposition. *Nanotechnology.* 2015;26(9):094002.

58. Eswar NKR, Singh SA, Heo J. Atomic layer deposited photocatalysts: comprehensive review on viable fabrication routes and reactor design approaches for photo-mediated redox reactions. *J Mater Chem A*. 2019;7(30):17703-17734. doi:10.1039/C9TA04780H
59. Weber M, Tuleushova N, Zgheib J, et al. Enhanced electrocatalytic performance triggered by atomically bridged boron nitride between palladium nanoparticles and carbon fibers in gas-diffusion electrodes. *Appl Catal B Environ*. 2019;257:117917. doi:10.1016/j.apcatb.2019.117917
60. Vempati S, Ranjith KS, Topuz F, Biyikli N, Uyar T. Electrospinning Combined with Atomic Layer Deposition to Generate Applied Nanomaterials: A Review. *ACS Appl Nano Mater*. 2020;3(7):6186-6209. doi:10.1021/acsanm.0c01120
61. Barhoum A, Pal K, Rahier H, Uludag H, Kim IS, Bechelany M. Nanofibers as new-generation materials: From spinning and nano-spinning fabrication techniques to emerging applications. *Appl Mater Today*. 2019;17:1-35. doi:10.1016/j.apmt.2019.06.015
62. Pasini SM, Valério A, Yin G, et al. An overview on nanostructured TiO₂-containing fibers for photocatalytic degradation of organic pollutants in wastewater treatment. *J Water Process Eng*. 2021;40:101827. doi:10.1016/j.jwpe.2020.101827
63. Mozzaquatro S, Valério A, Guelli SMA, et al. Journal of Environmental Chemical Engineering Plasma-modified TiO₂ / polyetherimide nanocomposite fibers for photocatalytic degradation of organic compounds. 2019;7(June):2-11. doi:10.1016/j.jece.2019.103213
64. Tang Q, Meng X, Wang Z, Zhou J, Tang H. One-step electrospinning synthesis of TiO₂/g-C₃N₄ nanofibers with enhanced photocatalytic properties. *2nd Int Workshop Graphene C₃N₄-Based Photocatal*. 2018;430:253-262. doi:10.1016/j.apsusc.2017.07.288
65. Basavarajappa PS, Patil SB, Ganganagappa N, Reddy KR, Raghu AV, Reddy ChV. Recent progress in metal-doped TiO₂, non-metal doped/codoped TiO₂ and TiO₂ nanostructured hybrids for enhanced photocatalysis. *2nd Int Conf Sustain Environ Energy ICSEE-2019*. 2020;45(13):7764-7778. doi:10.1016/j.ijhydene.2019.07.241
66. Shende TP, Bhanvase BA, Rathod AP, Pinjari DV, Sonawane SH. Sonochemical synthesis of Graphene-Ce-TiO₂ and Graphene-Fe-TiO₂ ternary hybrid photocatalyst nanocomposite and its application in degradation of crystal violet dye. *Ultrason Sonochem*. 2018;41:582-589. doi:10.1016/j.ultsonch.2017.10.024
67. Meng A, Zhang L, Cheng B, Yu J. TiO₂-MnO_x-Pt Hybrid Multiheterojunction Film Photocatalyst with Enhanced Photocatalytic CO₂-Reduction Activity. *ACS Appl Mater Interfaces*. 2019;11(6):5581-5589. doi:10.1021/acsami.8b02552
68. Nasr M, Eid C, Habchi R, Miele P. Recent Progress on Titanium Dioxide Nanomaterials for Photocatalytic Applications. Published online 2018:3023-3047. doi:10.1002/cssc.201800874

69. Chronakis IS. Novel nanocomposites and nanoceramics based on polymer nanofibers using electrospinning process — A review. 2005;167:283-293. doi:10.1016/j.jmatprotec.2005.06.053
70. Reneker DH, Yarin AL. Electrospinning jets and polymer nanofibers. *Polym Aligned Carbon Nanotub Act Compos Mater*. 2008;49(10):2387-2425. doi:10.1016/j.polymer.2008.02.002
71. Merenda A, Weber M, Bechelany M, et al. Fabrication of Pd-TiO₂ nanotube photoactive junctions via Atomic Layer Deposition for persistent pesticide pollutants degradation. *Appl Surf Sci*. 2019;483:219-230. doi:10.1016/j.apsusc.2019.03.285
72. Weber M, Drobek M, Rebière B, et al. Hydrogen selective palladium-alumina composite membranes prepared by Atomic Layer Deposition. *J Membr Sci*. 2020;596:117701. doi:https://doi.org/10.1016/j.memsci.2019.117701
73. Weber M, Kim JH, Lee JH, et al. High-Performance Nanowire Hydrogen Sensors by Exploiting the Synergistic Effect of Pd Nanoparticles and Metal–Organic Framework Membranes. *ACS Appl Mater Interfaces*. 2018;10(40):34765-34773. doi:10.1021/acsami.8b12569
74. Molenaar R, Jaap J, Zijp JR. Determination of Kubelka–Munk scattering and absorption coefficients by diffuse illumination. *Appl Opt*. 1999;38(10):2068-2077.
75. Konstantinou IK, Albanis TA. TiO₂-assisted photocatalytic degradation of azo dyes in aqueous solution: kinetic and mechanistic investigations: A review. *Appl Catal B Environ*. 2004;49(1):1-14. doi:10.1016/j.apcatb.2003.11.010
76. Konstantinou IK, Albanis TA. Photocatalytic transformation of pesticides in aqueous titanium dioxide suspensions using artificial and solar light: intermediates and degradation pathways. *Appl Catal B Environ*. 2003;42(4):319-335. doi:10.1016/S0926-3373(02)00266-7
77. Xuan T, Le H, Nguyen T Van, et al. Chemosphere Correlation between degradation pathway and toxicity of acetaminophen and its by-products by using the electro-Fenton process in aqueous media. 2017;172:1-9. doi:10.1016/j.chemosphere.2016.12.060
78. El Kateb M, Trelu C, Darwich A, et al. Electrochemical advanced oxidation processes using novel electrode materials for mineralization and biodegradability enhancement of nanofiltration concentrate of landfill leachates. *Water Res*. 2019;162:446-455.
79. Spurr RA, Myers H. Quantitative analysis of anatase-rutile mixtures with an X-ray diffractometer. *Anal Chem*. 1957;29(5):760-762.
80. Xu Q. *Nanoporous Materials: Synthesis and Applications*. CRC press; 2013.
81. Li H, Zhang W, Pan W. Enhanced Photocatalytic Activity of Electrospun TiO₂ Nanofibers with Optimal Anatase/Rutile Ratio. *J Am Ceram Soc*. 2011;94(10):3184-3187. doi:10.1111/j.1551-2916.2011.04748.x

82. Fan X xing, Yu T, Zhang L zhi, Chen X yi, Zou Z gang. Photocatalytic degradation of acetaldehyde on mesoporous TiO₂: Effects of surface area and crystallinity on the photocatalytic activity. *Chin J Chem Phys*. 2007;20(6):733.
83. Zhang C, Li Y, Wang Y, He H. Sodium-Promoted Pd/TiO₂ for Catalytic Oxidation of Formaldehyde at Ambient Temperature. *Environ Sci Technol*. 2014;48(10):5816-5822. doi:10.1021/es4056627
84. Ouyang W, Liu S, yao K, et al. Ultrafine hollow TiO₂ nanofibers from core-shell composite fibers and their photocatalytic properties. *Compos Commun*. 2018;9:76-80. doi:10.1016/j.coco.2018.06.006
85. Kawrani S, Nada AA, Bekheet MF, et al. Enhancement of calcium copper titanium oxide photoelectrochemical performance using boron nitride nanosheets. *Chem Eng J*. 2020;389:124326. doi:10.1016/j.cej.2020.124326
86. Nada AA, El Rouby WMA, Bekheet MF, et al. Highly textured boron/nitrogen co-doped TiO₂ with honeycomb structure showing enhanced visible-light photoelectrocatalytic activity. *Appl Surf Sci*. 2020;505:144419. doi:10.1016/j.apsusc.2019.144419
87. Bolokang AS, Motaung DE, Arendse CJ, Muller TFG. Morphology and structural development of reduced anatase-TiO₂ by pure Ti powder upon annealing and nitridation: Synthesis of TiO_x and TiO_xN_y powders. *Mater Charact*. 2015;100:41-49. doi:10.1016/j.matchar.2014.11.026
88. Zhang M, Lu D, Yan G, Wu J, Yang J. Fabrication of Mo+N-Codoped TiO₂ Nanotube Arrays by Anodization and Sputtering for Visible Light-Induced Photoelectrochemical and Photocatalytic Properties. Zhu S, ed. *J Nanomater*. 2013;2013:648346. doi:10.1155/2013/648346
89. Byrne C, Fagan R, Hinder S, McCormack DE, Pillai SC. New approach of modifying the anatase to rutile transition temperature in TiO₂ photocatalysts. *RSC Adv*. 2016;6(97):95232-95238. doi:10.1039/C6RA19759K
90. Yilmaz P, Lacerda AM, Larrosa I, Dunn S. Photoelectrocatalysis of Rhodamine B and Solar Hydrogen Production by TiO₂ and Pd/TiO₂ Catalyst Systems. *Electrochimica Acta*. 2017;231:641-649. doi:10.1016/j.electacta.2017.02.035
91. Iatsunskiy I, Pavlenko M, Viter R, et al. Tailoring the Structural, Optical, and Photoluminescence Properties of Porous Silicon/TiO₂ Nanostructures. *J Phys Chem C*. 2015;119(13):7164-7171. doi:10.1021/acs.jpcc.5b01670
92. Safajou H, Khojasteh H, Salavati-Niasari M, Mortazavi-Derazkola S. Enhanced photocatalytic degradation of dyes over graphene/Pd/TiO₂ nanocomposites: TiO₂ nanowires versus TiO₂ nanoparticles. *J Colloid Interface Sci*. 2017;498:423-432. doi:10.1016/j.jcis.2017.03.078

93. Levchuk I, Guillard C, Dappozze F, Parola S, Leonard D, Sillanpää M. Photocatalytic activity of TiO₂ films immobilized on aluminum foam by atomic layer deposition technique. *J Photochem Photobiol Chem*. 2016;328:16-23. doi:10.1016/j.jphotochem.2016.03.034
94. Serpone N. Relative photonic efficiencies and quantum yields in heterogeneous photocatalysis. *J Photochem Photobiol Chem*. 1997;104(1):1-12. doi:10.1016/S1010-6030(96)04538-8
95. Singh J, Tripathi N, Mohapatra S. Synthesis of Ag–TiO₂ hybrid nanoparticles with enhanced photocatalytic activity by a facile wet chemical method. *Nano-Struct Nano-Objects*. 2019;18:100266. doi:10.1016/j.nanoso.2019.100266
96. Khan H, Rigamonti MG, Boffito DC. Enhanced photocatalytic activity of Pt-TiO₂/WO₃ hybrid material with energy storage ability. *Appl Catal B Environ*. 2019;252:77-85. doi:10.1016/j.apcatb.2019.04.019
97. Leong KH, Chu HY, Ibrahim S, Saravanan P. Palladium nanoparticles anchored to anatase TiO₂ for enhanced surface plasmon resonance-stimulated, visible-light-driven photocatalytic activity. *Beilstein J Nanotechnol*. 2015;6(1):428-437.
98. Chan CC, Chang CC, Hsu WC, Wang SK, Lin J. Photocatalytic activities of Pd-loaded mesoporous TiO₂ thin films. *Chem Eng J*. 2009;152(2):492-497. doi:10.1016/j.cej.2009.05.012
99. Zhang X, Wu F, Wu X, Chen P, Deng N. Photodegradation of acetaminophen in TiO₂ suspended solution. *J Hazard Mater*. 2008;157(2):300-307. doi:10.1016/j.jhazmat.2007.12.098
100. Luna MDG de, Veciana ML, Su CC, Lu MC. Acetaminophen degradation by electro-Fenton and photoelectro-Fenton using a double cathode electrochemical cell. *J Hazard Mater*. 2012;217-218:200-207. doi:https://doi.org/10.1016/j.jhazmat.2012.03.018
101. Vo HNP, Le GK, Nguyen TMH, et al. Acetaminophen micropollutant: Historical and current occurrences, toxicity, removal strategies and transformation pathways in different environments. *Chemosphere*. 2019;236:124391. doi:https://doi.org/10.1016/j.chemosphere.2019.124391
102. Le TXH, Nguyen TV, Yacouba ZA, et al. Correlation between degradation pathway and toxicity of acetaminophen and its by-products by using the electro-Fenton process in aqueous media. *Chemosphere*. 2017;172:1-9. doi:https://doi.org/10.1016/j.chemosphere.2016.12.060
103. Nasr O, Mohamed O, Al-Shirbini AS, Abdel-Wahab AM. Photocatalytic degradation of acetaminophen over Ag, Au and Pt loaded TiO₂ using solar light. *J Photochem Photobiol Chem*. 2019;374:185-193. doi:10.1016/j.jphotochem.2019.01.032

104. Aguilar CA, Montalvo C, Ceron JG, Moctezuma E. Photocatalytic Degradation of Acetaminophen. *Int J Environ Res*. 2011;5(4):1071-1078. doi:10.22059/ijer.2011.465
105. Aguilar CA, Montalvo C, Zermeño BB, et al. Photocatalytic degradation of acetaminophen, tergitol and nonylphenol with catalysts TiO₂/Ag under UV and Vis light. *Int J Environ Sci Technol*. 2019;16(2):843-852. doi:10.1007/s13762-018-1707-x
106. Lin JCT, de Luna MDG, Aranzamendez GL, Lu MC. Degradations of acetaminophen via a K₂S₂O₈-doped TiO₂ photocatalyst under visible light irradiation. *Chemosphere*. 2016;155:388-394. doi:10.1016/j.chemosphere.2016.04.059
107. Ni G, Li Y, Wang S, Li Q. Construction of 1D/2D BN/TiO₂ nanostructures for efficient photocatalytic degradation of dyes. *Mater Lett*. 2021;288:129385. doi:10.1016/j.matlet.2021.129385
108. Czech B, Tysczuk-Rotko K. Visible-light-driven photocatalytic removal of acetaminophen from water using a novel MWCNT-TiO₂-SiO₂ photocatalysts. *Sep Purif Technol*. 2018;206:343-355. doi:10.1016/j.seppur.2018.06.025
109. Khasawneh OFS, Palaniandy P, Ahmadipour M, Mohammadi H, Bin Hamdan MR. Removal of acetaminophen using Fe₂O₃-TiO₂ nanocomposites by photocatalysis under simulated solar irradiation: Optimization study. *J Environ Chem Eng*. 2021;9(1):104921. doi:10.1016/j.jece.2020.104921
110. Kurniawan TA, Yanyan L, Ouyang T, Albadarin AB, Walker G. BaTiO₃/TiO₂ composite-assisted photocatalytic degradation for removal of acetaminophen from synthetic wastewater under UV-vis irradiation. *Semicond Mater Green Energy Environ Appl*. 2018;73:42-50. doi:10.1016/j.mssp.2017.06.048
111. Cheshme Khavar AH, Moussavi G, Mahjoub AR. The preparation of TiO₂@rGO nanocomposite efficiently activated with UVA/LED and H₂O₂ for high rate oxidation of acetaminophen: Catalyst characterization and acetaminophen degradation and mineralization. *Appl Surf Sci*. 2018;440:963-973. doi:10.1016/j.apsusc.2018.01.238
112. Yanyan L, Kurniawan TA, Ying Z, Albadarin AB, Walker G. Enhanced photocatalytic degradation of acetaminophen from wastewater using WO₃/TiO₂/SiO₂ composite under UV-VIS irradiation. *J Mol Liq*. 2017;243:761-770. doi:10.1016/j.molliq.2017.08.092
113. Ramasundaram S, Yoo HN, Song KG, Lee J, Choi KJ, Hong SW. Titanium dioxide nanofibers integrated stainless steel filter for photocatalytic degradation of pharmaceutical compounds. *J Hazard Mater*. 2013;258-259:124-132. doi:10.1016/j.jhazmat.2013.04.047